

Comparison of Simulated Polarimetric Signatures in Idealized Supercell Storms using Two-moment Bulk Microphysics Schemes in WRF

Marcus Johnson^{1,2}, Youngsun Jung¹, Daniel Dawson¹, and Ming Xue^{1,2}

¹Center for Analysis and Prediction of Storms and
²School of Meteorology
University of Oklahoma, Norman, OK 73072, USA

Submitted to Mon. Wea. Rev.
June 2015
Revised October 2015

*Corresponding Author Address:
Youngsun Jung,
CAPS, University of Oklahoma,
NWC Suite 2500
120 David Boren Blvd, Norman OK 73072
E-mail: youngsun.jung@ou.edu

Abstract

Microphysics parameterization becomes increasingly important as the model grid-spacing increases toward convection-resolving scales. The performance of several partially or fully two-moment (2M) schemes within the Weather Research and Forecast (WRF) model Version 3.5.1, chosen because of their well-documented advantages over one-moment (1M) schemes, is evaluated with respect to their ability in producing the well-known polarimetric radar signatures found within supercell storms. Such signatures include the Z_{DR} and K_{DP} columns, the Z_{DR} arc, the midlevel Z_{DR} and ρ_{HV} rings, the hail signature in the forward flank downdraft, and the K_{DP} foot. Polarimetric variables are computed from WRF model output using a polarimetric radar simulator. It is found that microphysics schemes with a 1M rimed-ice category are unable to simulate the Z_{DR} arc, despite containing a 2M rain category. It is also found that a hail-like rimed-ice category (in addition to graupel) is necessary to reproduce the observed hail signature. For the microphysics schemes that only contain a graupel-like rimed-ice category, only very wet graupel particles are able to reach the lowest model level, which did not adequately reduce Z_{DR} in this signature. The most realistic signatures overall are found with microphysics schemes that are fully 2M with a separate hail category.

1. Introduction

Realistic simulations of supercell storm structure and precipitation rely heavily on accurate treatment of cloud and precipitation microphysical processes. The two main approaches of modeling those processes employ 1) spectral bin (e.g., Khain et al. 2004) and 2) bulk microphysics parameterization (BMP) schemes (e.g., Lin et al. 1983; Milbrandt and Yau 2005b; a, hereafter MY05a,b respectively). The spectral bin scheme is generally more flexible because the hydrometeor particle size distribution (PSD) is discretized into bins commonly sorted by mass or diameter and explicitly predicted without assuming an underlying functional form, but bin schemes are computationally very expensive. For this reason, BMP schemes are used almost exclusively in real-time forecasts where microphysics parameterization is needed. BMP schemes typically assume a functional form of the PSD (although at least one BMP scheme predicts moments related to observed variables without an underlying PSD, see Kogan and Belochitski 2012). The most commonly assumed PSD function is the gamma distribution:

$$N(D) = N_0 D^\alpha \exp(-\Lambda D), \quad (1)$$

where N_0 , Λ , and α are the intercept, slope, and shape parameters, respectively, of the gamma distribution while D is the particle diameter. With the gamma PSD, physical quantities such as mixing ratio and total number concentration can be related to various moments of the PSD. Specifically, the n^{th} moment of the gamma PSD is given by

$$M(n) = \int_0^\infty D^n N(D) dD = \frac{N_0 \Gamma(\alpha + n + 1)}{\Lambda^{\alpha + n + 1}}, \quad (2)$$

where $\Gamma(n)$ is the gamma function.

Accordingly, microphysics schemes are commonly referred to by the number of distinct moments they predict for a given hydrometeor category (i.e., a scheme that predicts one moment of the PSD is a single-moment/one-moment [1M] scheme). 1M microphysics schemes usually predict mass mixing ratio q , which is proportional to the third moment for spherical hydrometeors (e.g., Kessler 1969; Lin et al. 1983; Rutledge and Hobbs 1983; Tao and Simpson 1993; Straka and Mansell 2005). Typically, double-moment (2M) schemes additionally predict total number concentration N_t (the zeroth moment), though the number of hydrometeor categories with predicted N_t varies by scheme (e.g., Ziegler 1985; Cotton et al. 1986; Ferrier 1994; Meyers et al. 1997; Cohard and Pinty 2000; Thompson et al. 2008; Morrison et al. 2009; Mansell et al. 2010). Triple-moment (3M) schemes that additionally predict the radar reflectivity factor Z (proportional to the 6th moment) have also been developed (Milbrandt-Yau (MY3): MY05a,b; Ziegler Variable Density (ZVD): Dawson et al. 2014, hereafter D14), which carry an increased computational cost with the additional predicted moment.

Multi-moment microphysics schemes that predict two or more moments consistently outperform 1M schemes in convective storm simulations. Specifically, recent studies (Milbrandt and Yau 2006; Dawson et al. 2010; Dawson et al. 2015b) produced better storm structure and cold pool characteristics using the 2M and 3M versions of the MY05a,b scheme than the 1M version. Additional studies (e.g., Wacker and Seifert 2001; MY05a; Dawson et al. 2010; Jung et al. 2010b, hereafter J10; Milbrandt and McTaggart-Cowan 2010) have shown that sedimentation in 1M schemes lacks a size-sorting effect, owing to the use of a single moment-weighted fall speed for the entire distribution of a given hydrometeor. Size sorting is a fundamental microphysical mechanism and one that is particularly important in supercell thunderstorms (e.g., Kumjian and Ryzhkov 2008; Kumjian and Ryzhkov 2009, hereafter KR08 and KR09

respectively; D14; Dawson et al. 2015a). In Jung et al. (2012), the structure and magnitude of analyzed polarimetric variables for a supercell storm were more similar to observations with the use of a 2M scheme than with a 1M scheme. Based on these studies, more recent studies at the convective scale (horizontal resolution $\leq 4\text{km}$; Weisman et al. 1997) are using 2M schemes (e.g., J10; Dawson et al. 2012; Mansell and Ziegler 2013; Potvin et al. 2013; Putnam et al. 2014).

Currently, various complex 2M microphysics schemes (e.g., MY05a,b; Thompson et al. 2008; Lim and Hong 2010; Mansell et al. 2010) are available to convection-resolving numerical weather prediction (NWP) models. It is common for different microphysics schemes to represent the same hydrometeor characteristics with different formulations (e.g., Morrison and Milbrandt 2011, hereafter MM11; Molthan and Colle 2012; Van Weverberg et al. 2013), and certain schemes contain microphysical conversion processes that are not included in others. For example, the Morrison scheme (Morrison et al. 2009) contains cloud droplet collection by cloud ice while the Milbrandt-Yau scheme (MY05a,b) does not (Van Weverberg et al. 2012). Although some microphysics schemes include both hail-like and graupel-like rimed-ice hydrometeors as separate categories (e.g., MY05a,b; Mansell et al. 2010), most schemes only contain a single rimed-ice hydrometeor category (e.g., Lin et al. 1983; Rutledge and Hobbs 1984; Hong and Lim 2006; Thompson et al. 2008; Morrison et al. 2009; Lim and Hong 2010). Understanding the behaviors and biases of microphysics schemes are important for proper use of such schemes as well as for improving the schemes.

Radar reflectivity is commonly used to evaluate model performance, but with the increased number of prognostic variables associated with multi-moment microphysics schemes and often additional hydrometeor types, reflectivity alone becomes insufficient (Jung et al. 2010a; Xue et al. 2010a). Polarimetric radar variables can be very useful because they can provide additional information on the size distribution, total amount, phase, and type of hydrometeors present. Briefly, differential reflectivity Z_{DR} is the ratio of return power at horizontal and vertical polarizations, and is related to the shape of scatterers. Cross-correlation coefficient ρ_{HV} is the correlation of horizontally- and vertically-polarized pulses within the radar resolution volume and is influenced by the complexity of the scatterer's shape and phase composition. Finally, specific differential phase K_{DP} is the difference of phase shift between the horizontally- and vertically-polarized pulses travelling through a medium over a given distance, and is sensitive to the mass of the medium (e.g., rain, hail, etc.).

This study attempts to gain understanding of the difference in the behaviors of several microphysics schemes available in the Weather Research and Forecasting (WRF) model (Skamarock et al. 2008) by examining simulated polarimetric radar variables and comparing hydrometeor frequency distributions between the microphysics schemes. We focus on the 2M (partially or fully) schemes available within WRF (version 3.5.1). Such simulations and comparisons can be especially useful to model developers to help them understand the behaviors of microphysics parameterization schemes. For example, Recent studies (e.g., J10; Kumjian and Ryzhkov 2012; D14) have used simulated radar observations to show the performance of the microphysics schemes depending on the predicted moments.

An idealized supercell thunderstorm is chosen for this study because of the prominent and well-documented polarimetric signatures present in such storms, some of which are listed in Table 1. In this paper, we focus on the simulated Z_{DR} and K_{DP} columns, Z_{DR} arc, midlevel Z_{DR} and ρ_{HV} rings, hail signature in the forward flank downdraft, and K_{DP} foot by the microphysics schemes in supercells following J10. Briefly, the Z_{DR} and K_{DP} columns are regions of enhanced Z_{DR} and K_{DP} associated with strong updrafts. The increase in Z_{DR} is from large raindrops and wet

rimed ice, while the increase in K_{DP} is due to water mass from shed raindrops and wet rimed ice. The Z_{DR} arc is an area of enhanced Z_{DR} near the surface due to size sorting of rimed ice and raindrops, which result in large raindrops (high Z_{DR}) on the southern edge of the right-moving supercell. The Z_{DR} and ρ_{HV} rings are ring-like patterns of enhanced Z_{DR} and depressed ρ_{HV} in the midlevels near the updraft due to large raindrops and wet rimed ice. The hail signature in the forward flank downdraft is an area of low Z_{DR} near the surface due to dry hail. Lastly, the K_{DP} foot is a region of enhanced K_{DP} near the surface, typically due to melting hail. Since these polarimetric signatures are significantly influenced by microphysical processes, the presence and magnitude of each simulated signature provide a basis for evaluating the performance of microphysics schemes and their ability to replicate these processes in simulations. Being able to replicate these processes and signatures is also crucial to direct assimilation of polarimetric radar data into convective-scale NWP models, since the update to the model state variables by these observations rely on properly simulated linkages between the observed quantities with the model states within the assimilating model. Weaknesses and shortcomings in the ability of the microphysics schemes to simulate these signatures are identified and discussed in this paper.

The rest of the paper is organized as follows. The simulation model configurations and the polarimetric simulator are first discussed in section 2, polarimetric signatures using different microphysics schemes are discussed in section 3, hydrometeor distributions are discussed in section 4, and conclusions are given in section 5.

2. Numerical simulations and polarimetric radar data simulator

a. Model configuration

The WRF-ARW v3.5.1 model is employed for idealized supercell storm simulations in this study. The model configuration is detailed in Table 2 and is based on that in MM11, which also compared the use of different microphysics schemes (albeit limited to two) in idealized supercell simulations. The horizontal grid spacing is 1 km while the vertical grid spacing is approximately 500 m. No radiation, land surface, cumulus, or planetary boundary layer parameterization schemes are employed for simplicity. The thermodynamic component of the WRF idealized supercell sounding follows Weisman and Klemp (1982). The vertical wind profile contains veering winds with shear of $5.15 \times 10^{-3} \text{ s}^{-1}$ for $z = 0.25\text{-}2.75$ km and unidirectional horizontal shear equal to $5.4 \times 10^{-3} \text{ s}^{-1}$ above for $z = 2.75\text{-}7.25$ km. An ellipsoidal thermal bubble with horizontal and vertical radii of 10 km and 1.5 km respectively initializes convection with a maximum potential temperature perturbation θ' (with respect to the environmental sounding) of 3 K at the center of the bubble. The bubble is centered at $z = 1.5$ km and in the middle of the horizontal domain. For further details, the reader is referred to MM11.

b. Microphysics schemes

Five partially or completely 2M schemes in the WRF model are evaluated in corresponding simulation experiments in this study: the Morrison (Morrison et al. 2009), Milbrandt-Yau (hereafter MY2 to distinguish from the 1M and 3M versions of the scheme;

MY05a,b), National Severe Storms Laboratory (hereafter NSSL; Mansell et al. 2010), Thompson (Thompson et al. 2008), and WRF double-moment 6-class (hereafter WDM6; Lim and Hong 2010) microphysics schemes. A brief description of the hydrometeor categories each scheme predicts is found in Table 3¹. Specifically, the MY2 and NSSL microphysics schemes are fully double-moment (2M) since these schemes each predict mass mixing ratio q and total number concentration N_i for each hydrometeor category. Additionally, these schemes contain a separate hail-like in addition to a graupel-like rimed ice category. The Morrison, Thompson, and WDM6 schemes only contain a graupel-like rimed ice category, and the graupel categories in the Thompson and WDM6 schemes are 1M. Further, the WDM6 scheme contains a fixed graupel intercept parameter (Hong and Lim 2006), while the Thompson scheme diagnoses graupel intercept parameter depending on its mixing ratio and the median volume diameter of supercooled rain (Morrison et al. 2015, hereafter M15). We note here that the namelist hail-switch option for the WSM6, WDM6, and Morrison schemes is available in WRFV3.6.1 that allows users to choose either graupel-like (default option) or hail-like parameters for the rimed-ice category but the option is not available in the 3.5.1 version used in this study. Since the Morrison, Thompson and WDM6 microphysics schemes are 2M for some categories and 1M for others, they are *partially* 2M. Additionally, the NSSL and WDM6 microphysics schemes used in this study predict number concentration of cloud condensation nuclei (CCN). For a comprehensive description of the microphysics schemes evaluated, the reader is referred to the appendix of M15. We point out that improvements and tuning are made to microphysics schemes frequently and therefore, the same schemes in different versions of WRF may produce differing results.

In order to create realistic polarimetric radar signatures, minor modifications are made to the MY2 scheme. The default MY2 scheme in WRF v3.5.1 contains a parameter named “Dh_min” for the mean mass diameter of hail set to 5 mm, which converts hail smaller than this threshold to graupel. This almost completely shuts down hail production in our supercell simulation, consistent with the results of Van Weverberg et al. (2012). Thus, for the MY2 experiment, “Dh_min” was set to 0 mm so that an adequate amount of hail can be produced. The original version of MY2 in MY05a,b did not contain this parameter.

c. Polarimetric radar data simulator

The polarimetric radar simulator described in J10 and the melting treatment described in D14 are used in this study in order to calculate polarimetric variables from WRF model output (i.e., predicted mass, and number concentration when applicable). The microphysics schemes used do not explicitly predict the water fraction of frozen particles, which is needed to properly compute their scattering amplitudes. In the schemes, melt water is removed from frozen particles during the forward integration and added to rainwater, leaving all frozen particles dry. Therefore, we emphasize that “melting” or “wet” frozen particles are simulated only by the polarimetric radar simulator, not within the microphysics schemes themselves.

For most of the microphysics schemes evaluated, the PSD for each hydrometeor species is generally described by an exponential distribution, which is a special case of the gamma PSD

¹ In WRF output, the prognostic number concentration is in mixing ratio units ($\# \text{ kg}^{-1}$).

given in Eq. (1) with the shape parameter α set to 0. There are a few exceptions to this. Snow in the Thompson scheme follows a PSD that is a linear combination of exponential and gamma distributions (Field et al. 2005; Thompson et al. 2008). Rain and snow hydrometeors in the NSSL scheme assume a mass-dependent gamma distribution (although in newer releases of the WRF model, rain follows a diameter-dependent distribution), and hail follows a gamma distribution with $\alpha = 1$ (for more details, the reader is referred to Mansell et al. 2010). Finally, rain in the WDM6 scheme follows a gamma distribution with $\alpha = 1$. Cloud droplets and cloud ice are currently not used in the simulator, although the inclusion of cloud ice is planned in the near future.

Each PSD is discretized in order to employ the T-matrix method (Waterman 1969; Vivekanandan et al. 1991) to calculate forward and backward scattering amplitudes of the rain, snow, graupel, and hail particles, so that Mie scattering effects can be accounted for in the simulation. To improve efficiency, the scattering amplitudes are pre-calculated and stored in lookup tables. We note here that the variability in snow parameterizations among the schemes are not included in the simulator. This may not be a major issue for supercell simulations as the contribution of snow to polarimetric signatures is much smaller than those from rain and/or graupel/hail. This should be improved when the simulator is applied to winter precipitation systems. From the calculated scattering amplitudes, Z_{DR} and K_{DP} are calculated following Zhang et al. (2001) and the formulation for cross-correlation coefficient ρ_{HV} can be found in J10. The simulator assumed the S-band wavelength in all calculations in this study.

At a given grid point, the mass of water available to attempt to saturate wet and melting snow, graupel, and hail is determined by the total rainwater mass. The percentage of rainwater available to each species is equal to the percentage of the individual frozen species' mass among the total mass of snow, graupel, and hail. The water fraction of snow is calculated as in J08. Graupel and hail water fraction is calculated using the iterative method of D14. This modification allows water fraction to vary across the rimed ice distributions, rather than using the single value water fraction across the distribution as in J08. This captures rimed ice characteristics (such as spherical hail tumbling or oblate hail with a water shell) for individual diameters, not just one characteristic for all particles. The water fraction treatment deviates slightly from D14 in that some of the available rainwater is first "soaked" into the graupel and hail distributions until the bulk density increases to 910 kg m^{-3} , then the soaked rainwater is assumed to be frozen. Next, the total critical water mass of the graupel/hail distribution, denoted as $q_{crit,g/h}$, is calculated by summing the maximum water mass allowed on the surface (i.e., the water "shell") of the graupel/hail over each diameter bin. For graupel/hail with diameter of 8 mm or less, the graupel/hail is assumed to be completely melted and water fraction is set to 1. Rain mass present in these rimed-ice diameter bins is returned to the rain field. For graupel/hail with diameter greater than 8 mm, the critical water mass that melting graupel/hail can hold on its shell prior to shedding is defined in Rasmussen and and (1987). If $q_{crit,g/h}$ is larger than the mass of rain available, $q_{crit,g/h}$ is set to the mass of rain available. Otherwise, $q_{crit,g/h}$ is added to $q_{g/h}$, the PSD is modified based on the new value of $q_{g/h}$, and iteration continues until $q_{crit,g/h}$ converges to a value. For those schemes that have 2M graupel and hail, mean mass diameter (D_m) is maintained by altering N_t . Mean mass diameter D_m of spherical hydrometeors is given by

$$D_m = \left(\frac{6\rho_a q}{\pi\rho N_t} \right)^{1/3}, \quad (3)$$

where ρ_a is the ambient air density and ρ is the bulk density of the hydrometeor. For those

schemes with 1M graupel, the corresponding fixed or diagnostic N_0 is used to update N_t . Additional details on the iterative procedure can be found in D14.

It should be noted that simulated polarimetric variables are sensitive to the shape and orientation of particles that have to be assumed in the simulator. As these parameters can vary quite a lot spatially and temporally among precipitation systems (e.g., Straka et al. 2000), the analyzed polarimetric signatures are not necessarily absolute, but still yield valid comparisons between the schemes. Rain axis ratio follows Brandes et al. (2002), dry rimed-ice axis ratio is derived from Knight (1986), and wet rimed-ice axis ratio is simulated as in D14. Rain mean canting angle and standard deviation of canting angle are set to 0° (Hendry and McCormick 1976), and snow mean canting angle and standard deviation of canting angle are set to 0° and 20° respectively. Rimed-ice mean canting angle is also set to 0° and standard deviation of canting angle varies with water fraction with a maximum of 60° assumed for dry rimed-ice as described in Jung et al. (2008, hereafter J08). This varying standard deviation of rimed-ice canting angle is meant to account for tumbling of dry hail (high standard deviation of canting angle), while wet hail (low standard deviation of canting angle) can be simulated as more stable. For more details, the reader is referred to J08.

3. Simulated polarimetric signatures

As observed polarimetric signatures are related to the microphysics and dynamics of the supercell storm, they are mostly present and persistent throughout the duration of a mature supercell (e.g., Hubbert et al. 1998; KR08; Romine et al. 2008). In our simulations, the maximum updraft speed reaches quasi-steady state by $t = 60$ min into the simulation, and thus enters its mature phase. With this in mind, polarimetric signatures are simulated from WRF output at $t = 100$ min except for the WDM6 scheme. Since the supercell storm in the WDM6 simulation takes longer to mature, the polarimetric signatures are not observed until $t = 120$ min. Thus, all microphysics schemes produce simulated polarimetric signatures (when present) as persistent as observed ones. Further, we focus our discussion of polarimetric signatures present in the right-moving cell, which is favored in a veering environmental wind shear (e.g., Klemp and Wilhelmson 1978; Rotunno and Klemp 1982; Klemp 1987).

First, we compare the simulated reflectivity at horizontal polarization, Z_H , at the first model level above ground (approximately 0.25 km) for various microphysics schemes (Fig. 1). Compared to other storms, the storm produced with the WDM6 scheme has weaker reflectivity and a smaller forward flank (FF) in general (Fig. 1e). This behavior is consistent with the results from the realtime storm-scale ensemble forecasts produced by the Center for the Analysis and Prediction of Storms (CAPS) for the 2013 NOAA Hazardous Weather Testbed (HWT) Spring Experiments (SEs) (e.g., Kong et al. 2007; Xue et al. 2007; Xue et al. 2008; Xue et al. 2010b; Kong et al. 2014) where the WDM6 scheme produced a persistently smaller stratiform rain area than other schemes. The overall structure is more similar to the supercell storm simulated with a 1M scheme in J10. We speculate that this is partly due to the fact that frozen species are 1M in the WDM6 scheme and the source of rain in stratiform rain is primarily from melting frozen particles (snow and graupel/hail). The low values of reflectivity could partly be due to no graupel reaching the lowest model level (Fig. 2m), as other scheme's reflectivity cores near the surface are generally co-located with nonzero rimed-ice mass (Fig. 2; Fig. 3).

For the remaining schemes, the MY2 and NSSL schemes produce the largest maximum values of Z_H , reaching 70-75 dBZ (Fig. 1b,c). This is due to the presence of large hail in the area

(Fig. 3). While the nonzero values of hail water fraction f_{wh} (Fig. 3c,f) indicate that the hail is wet, reflectivity does not appear to be particularly sensitive to water fraction values. The Thompson scheme also produces large maximum values of Z_H (Fig. 1d). Large amounts of medium-sized wet graupel (Fig. 2j,k,l) reaches the lowest model level, with the largest graupel found in the area with the largest Z_H . Medium-sized graupel with high water fraction (Fig. 2b,c) reaches the lowest model level in the Morrison scheme, but Z_H in this area (Fig. 1a) is relatively low compared to the other microphysics schemes' reflectivity cores co-located with rimed ice. This is due to the small amount of graupel reaching the lowest model level in the Morrison scheme, as q_g is less than 0.25 g kg^{-1} (Fig. 2a).

North-south vertical cross sections of reflectivity are taken through the region of maximum vertical velocity (i.e., updraft of the right-moving cell, Fig. 4) in each experiment. Locations of the vertical cross sections are indicated by the black lines in Fig. 1. The 0°C isotherm is shown to indicate the approximate melting level, and will be discussed further in subsequent sections. Reflectivity cores in the NSSL and Thompson schemes are much more intense than in the other schemes, with Z_H reaching 70-75 dBZ (Fig. 4g,j), and is due to relatively larger graupel in the Thompson scheme (Fig. 5k), and relatively larger hail in the NSSL scheme (Fig. 6c). The WDM6 scheme produces a very sharp gradient of reflectivity below 4 km in the updraft region, dropping from ~ 55 dBZ to ~ 30 dBZ (Fig. 4m). This is due to the absence of graupel below 4 km (Fig. 5n) where rain is small (Fig. 5m), although the sudden drop of reflectivity appears to be unphysical. The Morrison, MY2, and WDM6 schemes all produce similar and relatively smaller reflectivity maxima (Fig. 4a,d,m). These maxima are co-located with rimed ice, although the sizes of the rimed ice particles vary among the microphysics schemes. Small, wet graupel is found in this reflectivity maxima in the Morrison (Fig. 5b,c), MY2 (Fig. 5e,f), and WDM6 (Fig. 5n,o) schemes. Even though hail in the MY2 scheme (Fig. 6a,b) is larger than graupel in the Morrison, MY2, and WDM6 schemes, and reflectivity is heavily skewed towards larger hydrometeors (proportional to D^6), the similar reflectivities arise from the fact that the mixing ratio of graupel in the Morrison and WDM6 schemes is much larger than the mixing ratio of hail in the MY2 scheme (not shown), as reflectivity is still an additive calculation. Although rain and graupel sizes in the Morrison (Fig. 5a,b) and WDM6 (Fig. 5m,n) schemes are similar in the reflectivity maxima, graupel contributes to the reflectivity maxima slightly more than rain in these schemes (not shown). Thus, it is clear that the magnitude of the reflectivity core in each microphysics scheme is dictated by the size and amount of rimed ice.

a. Z_{DR} and K_{DP} columns

Large (and therefore oblate) raindrops and oblate wet rimed ice that have been advected above the melting layer by the convective updraft contribute to large Z_{DR} values in the Z_{DR} column (Illingworth et al. 1987; Conway and Zrnic 1993; Brandes et al. 1995; Loney et al. 2002). High liquid water mass from raindrops shed from either falling melting hail or hail experiencing wet growth, or water mass on the mixed-phased particles themselves, form a region of high K_{DP} located near the updraft referred to as the K_{DP} column (Hubbert et al. 1998; Loney et al. 2002).

All of the microphysics schemes examined produce the Z_{DR} and K_{DP} columns above the melting level (marked by the 0°C isotherm in the reflectivity plots in Fig. 4), though their magnitudes and depths vary considerably (Fig. 4). Locations of the vertical cross sections are indicated by the black lines in Fig. 1. Vertical velocity contours are included on the Z_{DR} and K_{DP} plots to denote the general updraft location. Z_{DR} contours are overlaid on the hydrometeor mean

mass diameter and water fraction plots in Fig. 5 and Fig. 6 to observe the hydrometeor characteristics in the Z_{DR} columns.

The overall Z_{DR} values in the column are the lowest in the NSSL scheme, with Z_{DR} of 0.5-2 dB (Fig. 4h), and highest in the Thompson scheme, with Z_{DR} of 3.5-4.5 dB (Fig. 4k). This can be explained by examining D_{mr} , $D_{mg,h}$, and rimed-ice water fraction ($f_{wg,h}$) (Fig. 5, Fig. 6). The relatively low Z_{DR} values of the NSSL scheme in the column is due to the presence of large hail with D_{mh} greater than 1 cm (Fig. 6c) that is dry (Fig. 6d). Large and rather dry hailstones reduce Z_{DR} because these particles can gyrate and tumble (e.g., Knight and Knight 1970; Thwaites et al. 1977; Rasmussen and and 1987), which would cause them to appear more spherical in shape on

$\hat{\sigma}$ $\hat{\sigma}$ $\hat{\sigma}$ overshadows the raindrops' contribution to Z_{DR} , given that the NSSL scheme actually produces relatively larger raindrops with D_{mr} exceeding 1 mm occasionally in the column (Fig. 5g). Raindrops become increasingly oblate as diameter increases, which increases Z_{DR} . Z_{DR} from wet graupel is significantly influencing the column more than rain in the Thompson scheme (not shown), as graupel in the column is relatively large with D_{mg} of 2-6 mm (Fig. 5k) and with high water fraction f_{wg} (Fig. 5l). However, the majority of raindrops are small with D_{mr} less than 0.75 mm (Fig. 5j). Medium-sized ($< \sim 1$ cm) wet hail and graupel produce large Z_{DR} values because of the liquid torus around the rimed-ice equator which aerodynamically stabilizes the particle (Rasmussen et al. 1984; Rasmussen and and 1987) and thus maintains an oblate shape. On the other hand, raindrops become increasingly spherical with decreasing diameter, reducing Z_{DR} . While the Z_{DR} column is dominated by rimed ice (Fig. 5; Fig. 6) in the NSSL and Thompson schemes, rain from melting rimed ice in the water fraction treatment (that does not necessarily appear in the D_{mr} fields) and rimed ice essentially contribute equally to these signatures in the Morrison MY2 scheme. WDM6 produces (on the whole) significantly large K_{DP} values of 8-10° km⁻¹ (Fig. 4l) in the K_{DP} column. While much larger K_{DP} values are sometimes observed for water-coated hail, typical values of K_{DP} range from 0 to 3° km⁻¹ at S-band (e.g., Straka et al. 2000; Schuur et al. 2003; Ryzhkov et al. 2005). K_{DP} columns are generally co-located with and sensitive to regions of relatively higher q_r (Fig. 7). Typically, liquid water mass on frozen hydrometeors are kept in their respective frozen hydrometeor mass fields as in Fig. 2 and Fig. 3, with the transferred water mass subtracted from the q_r field in order to treat q_r as pure rain. In this case, all liquid water mass (even on frozen hydrometers) is included in the q_r field for ease of comparison since K_{DP} is proportional to liquid water mass. The sensitivity of K_{DP} to liquid water mass on wet rimed ice is specifically evident in the WDM6 scheme, where K_{DP} values drop substantially from 4-5° km⁻¹ to 0-0.25° km⁻¹ (Fig. 4o) at model levels below the presence of wet graupel (Fig. 5n,o). This K_{DP} decrease can also be partially attributed to the presence of small raindrops (Fig. 5m), as K_{DP} is also related to the axis ratio of hydrometeors. While the Thompson scheme produces high values of q_r that are greater than 6 g kg⁻¹ in the K_{DP} column (Fig. 7d), D_{mr} is less than 0.75 mm (Fig. 5j). Since wet graupel (Fig. 5l) with D_{mg} ranging from 6 to 7 mm (Fig. 5k) is present for the largest K_{DP} values, the liquid water mass residing on wet graupel is responsible for the large K_{DP} values in the scheme. The MY2 scheme produces the lowest K_{DP} values in the column among the microphysics schemes, ranging from 0 to 1.5° km⁻¹ (Fig. 4f). This is a result of low liquid water mass q_r produced by the scheme(Fig. 7b).

Aside from the columns in the main updraft of the right mover, the WDM6 scheme exhibits a region of increased Z_{DR} and K_{DP} primarily below the melting layer in the left-moving cell, as shown in Fig. 4n,o. This increased Z_{DR} and K_{DP} is from somewhat oblate rain (Fig. 5m;

Fig. 7e) and wet graupel (Fig. 5n,o) near the updraft of the left-moving cell that is within this vertical cross section, and this appears to be physical. Another remarkable difference with the WDM6 scheme is the extremely low Z_{DR} and K_{DP} values near the surface (Fig. 4n,o) compared to the other schemes. This can be directly attributed to the relatively smaller max D_{mr} in the WDM6 scheme compared to the other schemes (Fig. 5m), and the lack of wet graupel reaching the lowest model level (Fig. 5n,o).

b. Z_{DR} arc

The Z_{DR} arc in a supercell storm is formed by the size sorting of hydrometeors by storm-relative winds (Ryzhkov et al. 2005; KR08; KR09; Kumjian and Ryzhkov 2012; Dawson et al. 2015a). Storm-relative winds advect hydrometeors as they fall through a given layer of the atmosphere, and a Z_{DR} gradient forms in the direction of the storm-relative mean wind (Dawson et al. 2015a) due to differing velocities of smaller (spherical) and larger (more oblate) hydrometeors. Focusing on the right mover in this section, the Z_{DR} arc is adjacent to the southern edge (Ryzhkov et al. 2005; KR08; KR09).

The simulated Z_{DR} arc seems to be primarily influenced by the size sorting of graupel and hail, rather than the size sorting of rain (D14). Consistent with the findings of D14, the Thompson and WDM6 schemes fail to produce a Z_{DR} arc, perhaps because they are 1M for the graupel species (Fig. 8g,i). On the other hand, the schemes that contain 2M rimed-ice categories (Morrison, MY2, and NSSL) are able to produce a Z_{DR} arc (Fig. 8a,c,e). The Z_{DR} arcs in the Morrison scheme are symmetric and have the highest Z_{DR} values, reaching 4.5 dB (Fig. 8a). In this area, D_{mr} is much larger (Fig. 8b) than in the Z_{DR} arcs of the MY2 and NSSL schemes. Qualitatively speaking, the NSSL scheme produces the location and structure of the Z_{DR} arc that compares most favorably with observations (e.g., KR08). The Z_{DR} arc in the NSSL scheme is located on the edge of the right-moving supercell (Fig. 8e), while the Z_{DR} arc in the MY2 scheme is slightly further into the forward flank (Fig. 8c). The Z_{DR} arc in the MY2 scheme is slightly stronger in magnitude than the Z_{DR} arc in the NSSL scheme due to wet hail in the MY2 Z_{DR} arc (Fig. 3b,c), although D_{mr} in the MY2 scheme is slightly larger (Fig. 8).

c. Midlevel Z_{DR} and ρ_{HV} rings

Midlevel Z_{DR} and ρ_{HV} rings exist because frozen hydrometeors melt as they fall around the updraft. Large raindrops and oblate, melting rimed ice around the updraft form a ring-shaped signature of high Z_{DR} , while melting hydrometeors that are large enough to encounter the resonance effect will substantially decrease ρ_{HV} (KR08). According to KR08, half-rings can also appear, and do so on the right flank of the updraft when present.

Since the vertical cross sections of reflectivity indicate the location of the melting level is around 4 km (Fig. 4), horizontal cross sections are taken at approximately 4 km to examine the midlevel Z_{DR} and ρ_{HV} rings (Fig. 9), with vertical velocity contours in the Z_{DR} plots indicating the updraft location. Z_{DR} contours are overlaid on the mean mass diameter and water fraction plots (Fig. 10; Fig. 11) to observe the hydrometeor characteristics in the Z_{DR} rings. The Morrison, MY2, and Thompson schemes produce the largest Z_{DR} magnitudes of 3.5-4.5 dB (Fig. 9a,c,g), while the WDM6 scheme produces the overall smallest Z_{DR} magnitudes of 0.5-3 dB in the simulated ring (Fig. 9i). The high Z_{DR} values in the Thompson scheme appear in a disk shape and do not show a distinct ring or half-ring structure (Fig. 9g) which is similar to those produced by the 1M scheme in J10. Schemes with the largest Z_{DR} values contain relatively larger raindrops in the overlaid Z_{DR} contours (Fig. 10a,d,j) and medium-sized, wet rimed ice (Fig. 10b,c,k,l; Fig.

11a,b) in the vicinity of the ring. Larger rain and wet rimed ice are oblate, which increases Z_{DR} . While D_{mr} in the WDM6 scheme is not small (Fig. 10m), small wet graupel (Fig. 10n,o) is unable to further increase Z_{DR} . Also of note, the NSSL scheme has relatively large, oblate raindrops (Fig. 10g) outside of the overlaid Z_{DR} contours (i.e., corresponding to lower Z_{DR}). This is due to the presence of large, dry hail (Fig. 11c,d) preventing larger Z_{DR} . Generally, a more realistic, almost complete Z_{DR} ring signature is simulated with the MY2 scheme (Fig. 9c). The WDM6 scheme is able to approximately simulate a complete Z_{DR} ring, but with very low Z_{DR} values on the bottom-right flank of the updraft (Fig. 9i). The Morrison and NSSL schemes are also able to produce a half-ring as has been observed (Fig. 9a,e).

J10 discussed in depth how hailstones that encounter the resonance effect can reduce ρ_{HV} (KR08; KR09). The resonance effect occurs in the Mie (or resonance) region where $D|\epsilon|^{1/2}/\lambda$ approaches 1. Here, ϵ is dielectric constant and λ is radar wavelength. In this region, the radar cross section of a particle oscillates as a function of particle size (or radar frequency) instead of increasing with increasing size. In J10, dry hailstones only marginally decrease ρ_{HV} , but only for very large hailstones. Large wet hailstones reduce ρ_{HV} , but the magnitude of the ρ_{HV} reduction decreases with increasing hail water fraction (although the size of resonance-sized hailstones also decreases). As discussed in section 2c, water fraction of rimed ice is computed by adding available water mass to the existing distributions of the rimed-ice mass categories (i.e., dry rimed ice and wet rimed ice do not coexist in separate distributions at a given location). Thus, it can be inferred with confidence that rimed ice with large D_m and moderate f_w can encounter the resonance effect in this study. The water fraction treatment in this study is different from the one in J08 and J10, which does allow for coexistence of dry and wet rimed ice in addition to pure liquid drops within the melting layer. The largest ρ_{HV} reduction in the midlevel ρ_{HV} rings is found with the NSSL scheme, with ρ_{HV} equal to 0.92-0.94 (Fig. 9f). The presence of relatively large hail that is partially wet (Fig. 11c,d) in that area suggests that resonance may play a big role. While the Morrison and Thompson schemes show a region of reduced ρ_{HV} values (Fig. 9b,h) to the left of the updraft, the MY2 and NSSL schemes produce better defined half-ring and full-ring shapes respectively (Fig. 9d,f) in the vicinity of the updraft compared to the other schemes. The WDM6 scheme is unable to reproduce a ρ_{HV} ring (Fig. 9j), suggesting that rimed-ice particles (Fig. 10n) produced by the scheme may be smaller than resonance sizes.

d. Hail signature in the forward flank downdraft

Because large, dry hailstones have the potential to tumble, as they reach the surface an area of low Z_{DR} will form (KR08). The NSSL scheme is the only scheme to produce the hail signature in the forward flank downdraft, which is centered at $x = 125$ km, $y = 85$ km in Fig. 8e. Large, dry hail (Fig. 3e,f) falls in this area and is associated with a region of reduced Z_{DR} (Fig. 8e). Graupel at the lowest model level in the Morrison and Thompson schemes is medium-sized (Fig. 2k,l), but also very wet (Fig. 2c,l), enhancing Z_{DR} . For the WDM6 scheme, no graupel reaches the lowest model level (Fig. 2n,o). The MY2 scheme has very little graupel near the surface (Fig. 2e,f), although widespread hail (Fig. 3b,c) is able to reach the lowest model level. Hail in the MY2 scheme is medium-sized and mostly melted (Fig. 3b,c), increasing Z_{DR} .

e. K_{DP} foot

The K_{DP} foot is a region of large K_{DP} near the surface that spans from the forward flank into the vicinity of the storm's hook region. High liquid water mass from melting hail increases

K_{DP} in this signature (Romine et al. 2008). As stated earlier, our discussion is focused on signatures found in the right mover. The magnitude of the K_{DP} foot is sensitive to q_r present (which includes liquid water mass on graupel and hail as in section 3a) at the lowest model level (Fig. 12). The Thompson scheme produces the largest K_{DP} values of $10\text{-}12^\circ \text{ km}^{-1}$ (Fig. 12g), while the Morrison, MY2, and WDM6 schemes produce the smallest K_{DP} values in the K_{DP} foot region, which do not exceed $0.75^\circ \text{ km}^{-1}$ (Fig. 12a,c,i). As stated in section 3a, typical K_{DP} values range from 0 to 3° km^{-1} . At the lowest model level, the Thompson scheme produces the largest q_r in the K_{DP} foot region (Fig. 12h), while the MY2 scheme produces the lowest q_r (Fig. 12d). Liquid water mass transferred to melting graupel in the Thompson scheme (Fig. 2k,l) in the K_{DP} foot region contributes to the large K_{DP} values. Max q_r in the Morrison scheme is comparable to max q_r in the NSSL scheme in the K_{DP} foot region (Fig. 12b,f), but larger D_{mr} in the NSSL scheme (Fig. 8) is able to increase K_{DP} more. Similarly, the WDM6 scheme produces relatively larger q_r (Fig. 12j) than the Morrison and MY2 schemes in the K_{DP} foot region, but given the relatively small raindrops at the lowest model level (Fig. 8j), K_{DP} is low for this scheme. Outside the hook, enhanced K_{DP} is found in the Morrison and MY2 schemes (Fig. 12b,c) to the left of the updraft. In the Morrison scheme, this is a result of high liquid mass from rain as there is no graupel in this area (Fig. 2a). In the MY2 scheme, this enhanced K_{DP} is primarily from liquid water mass on melting hail (Fig. 3b,c).

4. DSD properties

a. Properties of liquid hydrometeor

Contoured frequency by altitude diagrams (CFADs, Yuter and Houze 1995) (Fig. 13; Fig. 14) are made to gain an understanding of any potential biases in each microphysics scheme. The CFADs show the number of grid point occurrences, normalized by the total number of grid points that contain a non-zero mass, per 0.25 mm range of D_{mr} and D_{mg} and 0.5 mm range of D_{mh} at each model height level. The plots are normalized in order to provide a basis for comparing the frequency distributions since raw counts are affected by the size of the simulated supercell storm. M15 examined vertical distributions of median volume diameter D_0 of rain relative to a simulated squall line's leading edge for the microphysics schemes that are examined in this study, and found somewhat similar distributions. While median volume diameter is different than the mean mass diameter examined here, parallels can be made nonetheless.

It is seen that D_{mr} increases with progressively lower model heights near the surface much more for the Morrison and MY2 schemes (Fig. 13a,c) than other schemes. According to M15, these schemes can encounter excessive size sorting since the shape parameter α is 0 for the rain PSD. Excessive size sorting of hydrometeors in 2M schemes can occur when the hydrometeor PSD is represented with a constant shape parameter α (e.g., Wacker and Seifert 2001; MY05a; Milbrandt and McTaggart-Cowan 2010; Kumjian and Ryzhkov 2012). Further, raindrops in the Morrison scheme have the potential to reach the maximum raindrop size threshold in the scheme when the mass of rain is low without much resistance. This is because raindrop breakup is performed by reducing self-collection, and self-collection is only initiated beyond a mixing ratio threshold. The presence of D_{mr} greater than 1.75 mm with noticeable relative frequency that is found only in the Morrison scheme helps explain why this scheme produces the largest Z_{DR} and D_{mr} in the Z_{DR} arc near the surface (Fig. 8a,b). The remaining schemes do have gradually increasing D_{mr} with progressively lower model heights, and M15 offered explanations for the general lack of excessive size sorting present in these schemes. The

NSSL scheme modifies total number concentration N_t of rain, graupel, and hail to simulate more accurate reflectivity (Mansell 2010), which also helps control size sorting. Rain below the melting layer in the Thompson and WDM6 microphysics schemes are essentially dominated by one size bin (Fig. 13g,i). M15 noted a lack of excessive size sorting in the Thompson scheme, which results from increased number-weighted mean fall speed in the scheme as a strategy to reduce size sorting. The study was unable to pinpoint a reason for the WDM6 scheme's proclivity for small raindrops, but was consistent with the WDM6's rain distribution in this study.

The relative frequency maxima for the NSSL and Thompson schemes in the smallest bin (Fig. 13e,g) at the low levels appears to be the result of small raindrops forming from autoconversion in the presence of low level clouds, exhibited by the small D_{mr} near the updrafts seen in Fig. 8. Finally, the Morrison, NSSL, and Thompson schemes produce a secondary relative frequency above the melting level (Fig. 13a,e,g). Most of these small drops are likely a result of the updraft carrying supercooled water into upper levels, as the majority of rain at these levels is located near the updrafts. This signal is distinctly absent in the MY2 scheme (Fig. 13c). This is not indicative of a lack of supercooled raindrops, but rather a broad distribution of drops at each level with qualitatively smaller coverage than other schemes (not shown). Thus, this signal is not present. The WDM6 scheme shows a continuous maximum in the smallest bin extending above the melting layer, similar to the signals at low levels and above the melting layer previously discussed (Fig. 13i). Drops above the melting level are concentrated around the updraft and drops below the melting level could be the result of autoconversion, which is consistent with the other microphysics schemes that exhibit these signals. However, the large relative frequency in the smallest D_{mr} bin (Fig. 13i) shows small drops might be a bias of the WDM6 scheme.

b. Properties of frozen hydrometeors

Graupel and hail CFADs (Fig. 13; Fig. 14) are produced as in section 4a. In the graupel CFADs, several differences are present among the different microphysics schemes. Interestingly, there is a maximum in relative frequency near the surface in the 3.5-3.75 mm D_{mg} bin (Fig. 13b) in the Morrison scheme that extends vertically to approximately 6 km, and is connected to the maximum at lower diameters. This maximum is likely due to graupel reaching the maximum size threshold in the scheme, since D_{mg} rapidly increases with progressively lower model heights in the Morrison CFAD due to excessive size sorting. (Fig. 13b). Excessive size sorting can also be seen in the MY2 scheme, with D_{mg} rapidly increasing near the surface (Fig. 13d). Like the rain PSDs, the shape parameter α is 0 for the graupel PSDs in these schemes, which is likely responsible for the excessive size sorting. In the NSSL scheme (Fig. 13f), D_{mg} does increase with gradually lower model heights, but much less than the Morrison and MY2 schemes because of the N_t modification discussed in section 4a. In the Thompson and WDM6 schemes (Fig. 13h,j), D_{mg} weakly increases above the melting layer with progressively lower model heights. The graupel distribution also gets wider at lower heights for both schemes. This is because 1M schemes do not allow size sorting, so little size variation is found with height. The weak D_{mg} increase is solely due to increasing graupel mass. This helps explain why the Thompson and WDM6 schemes were unable to simulate a Z_{DR} arc, because this signature might be influenced more by the size sorting of rimed ice (D14). Graupel only reaches the lowest model level with noticeable relative frequency in the Morrison and Thompson schemes (Fig. 13b,h) and is simulated to be wet. This helps explain why graupel-only schemes are unable to reproduce the

hail signature, because small to medium-sized wet graupel (which is oblate) would actually increase Z_{DR} .

The greatest difference between the hail CFADs with the MY2 and NSSL schemes is the magnitude of the relative frequencies. The greatest range of magnitudes in the NSSL scheme is 0.0075-0.01 (Fig. 14b), while max magnitudes in the MY2 scheme range from 0.0425 to 0.045 (Fig. 14a). The most likely explanation for this is that frozen rain is included in the hail category in the MY2 scheme, while frozen rain is included in the graupel category in the NSSL scheme. In other words, the main source of hail is frozen rain in the MY2 scheme, while the main source of hail in the NSSL scheme is graupel undergoing wet growth, which explains the dominant hail size difference between the two schemes. Much larger hail is found in the NSSL CFAD near the surface than the MY2 CFAD (Fig. 14). This is consistent with results from section 3d, where large dry hail is able to form a hail signature in the NSSL scheme.

5. Summary and discussion

In this paper, we performed idealized supercell storm simulations with several two-moment (2M) microphysics schemes available in the WRF model. We aimed to 1) determine how well each microphysics scheme reproduces unique polarimetric signatures in supercell storms, 2) relate the presence and relative magnitude of these signatures to the characteristics of the hydrometeors produced by the microphysics scheme and 3) further investigate the behaviors and properties of each microphysics scheme through hydrometeor relative frequency distributions. Five fully or partially 2M schemes in the WRF model were evaluated, and polarimetric variables were calculated from the model output using an enhanced polarimetric radar simulator. Those five schemes were the Morrison, Milbrandt-Yau, NSSL, Thompson, and WDM6 schemes.

Here we summarize results and their corresponding conclusions for the microphysics schemes evaluated in the supercell storm simulations:

- 1) Each scheme is able to produce the Z_{DR} and K_{DP} columns, although the intensity of the columns varies significantly among the schemes. The Thompson scheme presents the strongest Z_{DR} and K_{DP} columns because of relatively larger graupel size with high liquid water content. The NSSL scheme produces a relatively weak Z_{DR} column because it produces hail that is generally too large to hold much water before it sheds and likely appears spherical to radar since it has the potential to tumble. The MY2 scheme produces the weakest K_{DP} column because of its smallest q_r values among schemes.
- 2) The Morrison, MY2, and NSSL schemes are able to simulate a Z_{DR} arc, with the NSSL scheme producing the most realistic signature. This is allowed by the 2M nature of their respective rimed-ice categories. The Morrison scheme produces higher Z_{DR} values in the arc than the other schemes due to relatively larger raindrops produced by the scheme. The Thompson and WDM6 schemes, which contain 1M rimed-ice categories, are unable to replicate a Z_{DR} arc because of the lack of rimed-ice size sorting.
- 3) Each microphysics scheme, except for the Thompson scheme, is able to simulate an enhanced, ring-like (full or half) mid-level Z_{DR} signature. The major contributors to the midlevel Z_{DR} ring are small to medium-sized wet rimed-ice particles along with relatively large raindrops, which have oblate shapes. However, small graupel particles contribute to the WDM6 scheme having the lowest overall Z_{DR} values. The presence and magnitude of the ρ_{hv} ring are related to the size of wet rimed ice, due to the resonance effect. All but the WDM6 scheme simulate a reduced ρ_{hv} area around the updraft, due to small graupel in the scheme

that does not encounter the resonance effect. The NSSL scheme reduces ρ_{hv} the most, as large dry hail in the scheme is likely dominated by the resonance effect.

- 4) The hail signature in the forward flank downdraft simulated in this study relies on the presence of large, dry hail at the surface, which reduces Z_{DR} . Microphysics schemes that only contain a graupel-like rimed-ice category fail to reproduce this signature. The graupel particles that do reach the lowest model level in these schemes are small to medium-sized with high water fraction, which increase Z_{DR} . In fact, only the NSSL scheme is able to reproduce this signature, due to large dry hail reaching the lowest model level. Hailstones near the surface in the MY2 scheme are small to medium-sized and wet, and thus fail to simulate the hail signature.
- 5) Each scheme is able to simulate the K_{DP} foot near the surface. The Thompson scheme produces the strongest K_{DP} foot primarily due to high liquid water mass residing on melting graupel. The Morrison, MY2, and WDM6 schemes produce the weakest K_{DP} foot, due to low liquid water mass in the MY2 scheme and relatively small drops in the Morrison and WDM6 schemes in the vicinity of this signature.
- 6) Excessive size sorting of raindrops near the surface is evident in the Morrison and MY2 CFADs, while the other schemes display more gradual size sorting. This is primarily due to the constant shape parameter of 0 in the Morrison and MY2 schemes, while the other schemes have strategies to inhibit size sorting (NSSL, Thompson), or are just dominated by small drops (WDM6). Particularly, the much larger drops present in the Morrison CFAD as a result of excessive size sorting help explain the largest Z_{DR} values in the Z_{DR} arc compared to the other schemes.
- 7) Graupel CFADs exhibit similar size sorting characteristic in the Morrison, MY2, and NSSL scheme as in the rain CFADs. The Thompson and WDM6 show a distinct lack of size sorting due to the 1M nature of the graupel category, which helps explain why the schemes were unable to simulate a Z_{DR} arc due to the signature's possible dependence on size sorting of rimed ice. The CFADs also show that among the graupel-only schemes, no large graupel that could be simulated as dry graupel reached the lowest model level, which helps explain why the graupel-only schemes were unable to simulate the hail signature. The much larger hail sizes in the NSSL CFAD help explain the ability of the scheme to replicate the hail signature, as smaller hail in the MY2 CFAD is simulated as wet.

The ability of microphysical schemes to reproduce observed polarimetric signatures is critical for direct assimilation of polarimetric measurements into convective-scale NWP models. If the model is unable to produce the information carried by observations, direct assimilation of such observations is unlikely to produce correct impacts as assimilation of such observations aims to reduce the difference between the simulated and observed information. For example, when graupel never reaches the ground in a certain microphysics scheme due to low density and slow terminal velocity assumptions, assimilating the hail signature will likely remove rain from the area and result in a hole in surface precipitation. Studies such as the current one can give us an idea as to whether or not a certain microphysics scheme needs improvement in particular aspects to allow for successful assimilation of polarimetric data.

Although this study is able to relate the presence of unique supercell polarimetric signatures to the hydrometeor PSD characteristics, further research is needed to explain the differences in particle size, mass, and spatial distributions between the microphysics schemes. In order to fully reproduce the polarimetric signatures, it appears a fully two-moment scheme is needed, especially for the large rimed-ice category. Further, the addition of a second, hail-like

rimed-ice category, or the tuning of the existing rimed-ice category to be more hail-like, might be necessary to adequately reproduce the hail signature. Additional comparisons between microphysics schemes for different types of convective systems can not only help users choose most suitable schemes for their purposes, but also help developers to identify weaknesses of and improve their schemes.

Acknowledgement This research was supported by a research grant of “Development of a Polarimetric Radar Data Simulator for Local Forecasting Model” by the Korea Meteorological Administration. Further support was provided by NSF grants AGS-1046171 and AGS-1261776.

References

- Brandes, E. A., G. Zhang, and J. Vivekanandan, 2002: Experiments in rainfall estimation with a polarimetric radar in a subtropical environment. *Journal of Applied Meteorology*, **41**, 674–685.
- Brandes, E. A., J. Vivekanandan, J. D. Tuttle, and C. J. Kessinger, 1995: A study of thunderstorm microphysics with multiparameter radar and aircraft observations. *Mon. Wea. Rev.*, **123**, 3129–3143.
- Cohard, J.-M. and J.-P. Pinty, 2000: A comprehensive two-moment warm microphysical bulk scheme. I: Description and tests. *Quart. J. Roy. Meteor. Soc.*, **126**, 1815–1842.
- Conway, J. W. and D. S. Zrnic, 1993: A study of embryo production and hail growth using dual-Doppler and multiparameter radars. *Mon. Wea. Rev.*, **121**, 2511–2528.
- Cotton, W. R., G. J. Tripoli, R. M. Rauber, and E. A. Mulvihill, 1986: Numerical simulation of the effects of varying ice crystal nucleation rates and aggregation processes on orographic snowfall. *J. Climate Appl. Meteor.*, **25**, 1658–1680.
- Dawson, D. T., E. R. Mansell, and M. R. Kumjian, 2015a: Does wind shear cause hydrometeor size sorting?. *J. Atmos. Sci.*, **72**, 340–348.
- Dawson, D. T., M. Xue, J. A. Milbrandt, and M. K. Yau, 2010: Comparison of evaporation and cold pool development between single-moment and multimoment bulk microphysics schemes in idealized simulations of tornadic thunderstorms. *Mon. Wea. Rev.*, **138**, 1152–1171.
- Dawson, D. T., L. J. Wicker, E. R. Mansell, and R. L. Tanamachi, 2012: Impact of the environmental low-level wind profile on ensemble forecasts of the 4 May 2007 Greensburg, Kansas, tornadic storm and associated mesocyclones. *Mon. Wea. Rev.*, **140**, 696–716.
- Dawson, D. T., M. Xue, J. A. Milbrandt, and A. Shapiro, 2015b: Sensitivity of real-data simulations of the 3 May 1999 Oklahoma City tornadic supercell and associated tornadoes to multimoment microphysics. Part I: Storm- and tornado-scale numerical forecasts. *Mon. Wea. Rev.*, 2241–2265.
- Dawson, D. T., E. R. Mansell, Y. Jung, L. J. Wicker, M. R. Kumjian, and M. Xue, 2014: Low-level ZDR signatures in supercell forward flanks: The role of size sorting and melting of hail. *J. Atmos. Sci.*, **71**, 276–299.
- Ferrier, B. S., 1994: A double-moment multiple-phase four-class bulk ice scheme. Part I: Description. *J. Atmos. Sci.*, **51**, 249–280.
- Field, P. R., R. J. Hogan, P. R. A. Brown, A. J. Illingworth, T. W. Choullarton, and R. J. Cotton, 2005: Parameterization of ice-particle size distributions for mid-latitude stratiform cloud. *Quart. J. Roy. Meteor. Soc.*, **131**, 1997–2017.

- Hendry, A. and G. C. McCormick, 1976: Radar observations of the alignment of precipitation particles by electrostatic fields in thunderstorms. *J. Geophys. Res.*, **81**, 5353–5357.
- Hong, S.-Y. and J.-O. J. Lim, 2006: The WRF single-moment 6-class microphysics scheme (WSM6). *J. Korean Meteor. Soc.*, **42**, 129–151.
- Hubbert, J., V. N. Bringi, L. D. Carey, and S. Bolen, 1998: CSU-CHILL Polarimetric Radar Measurements from a Severe Hail Storm in Eastern Colorado. *J. Appl. Meteor.*, **37**, 749–775.
- Illingworth, A. J., J. W. F. Goddard, and S. M. Cherry, 1987: Polarization radar studies of precipitation development in convective storms. *Quart. J. Roy. Meteor. Soc.*, **113**, 469–489.
- Jung, Y., G. Zhang, and M. Xue, 2008: Assimilation of simulated polarimetric radar data for a convective storm using the ensemble Kalman filter. Part I: Observation operators for reflectivity and polarimetric variables. *Mon. Wea. Rev.*, **136**, 2228–2245.
- Jung, Y., M. Xue, and G. Zhang, 2010a: Simultaneous estimation of microphysical parameters and the atmospheric state using simulated polarimetric radar data and an ensemble Kalman filter in the presence of an observation operator error. *Mon. Wea. Rev.*, **138**, 539–562.
- Jung, Y., M. Xue, and G. Zhang, 2010b: Simulations of polarimetric radar signatures of a supercell storm using a two-moment bulk microphysics scheme. *J. Appl. Meteor. Climatol.*, **49**, 146–163.
- Jung, Y., M. Xue, and M. Tong, 2012: Ensemble Kalman filter analyses of the 29–30 May 2004 Oklahoma tornadic thunderstorm using one- and two-moment bulk microphysics schemes, with verification against polarimetric radar data. *Mon. Wea. Rev.*, **140**, 1457–1475.
- Kessler, E., 1969: *On the Distribution and Continuity of Water Substance in Atmospheric Circulations*. Vol. 32, *Meteor. Monogr.*, 84 pp.
- Khain, A., A. Pokrovsky, M. Pinsky, A. Seifert, and V. Phillips, 2004: Simulation of effects of atmospheric aerosols on deep turbulent convective clouds using a spectral microphysics mixed-phase cumulus cloud model. Part I: Model description and possible applications. *J. Atmos. Sci.*, **61**, 2963–2982.
- Klemp, J. B., 1987: Dynamics of tornadic thunderstorms. *Annul Rev. Fluid. Mech.*, **19**, 369–402.
- Klemp, J. B. and R. B. Wilhelmson, 1978: Simulations of right- and left-moving thunderstorms produced through storm splitting. *J. Atmos. Sci.*, **35**, 1097–1110.
- Knight, C. A. and N. C. Knight, 1970: The falling behavior of hailstones. *J. Atmos. Sci.*, **27**, 672–681.
- Knight, N. C., 1986: Hailstone shape factor and its relation to radar interpretation of hail. *J. Climate Appl. Meteor.*, **25**, 1956–1958.
- Kogan, Y. L. and A. Belochitski, 2012: Parameterization of cloud microphysics based on full integral moments. *J. Atmos. Sci.*, **69**, 2229–2242.
- Kong, F., M. Xue, D. Bright, M. C. Coniglio, K. W. Thomas, Y. Wang, D. Weber, J. S. Kain, S. J. Weiss, and J. Du, 2007: Preliminary analysis on the real-time storm-scale ensemble forecasts produced as a part of the NOAA hazardous weather testbed 2007 spring experiment. *22nd Conf. Wea. Anal. Forecasting/18th Conf. Num. Wea. Pred.*, Salt Lake City, Utah, Amer. Meteor. Soc., CDROM 3B.2.
- Kong, F., M. Xue, K. W. Thomas, Y. Wang, K. Brewster, Y. Jung, A. J. Clark, M. C. Coniglio, J. C. Jr., I. L. Jirak, J. S. Kain, and S. J. Weiss, 2014: CAPS storm-scale ensemble forecasting system: Impact of IC and LBC perturbations. *26th Conf. on Weather Analysis and Forecasting/22nd Conf. on Numerical Weather Prediction*, Atlanta, GA, Amer. Meteor. Soc., 119.

- Kumjian, M. R. and A. V. Ryzhkov, 2008: Polarimetric signatures in supercell thunderstorms. *J. Appl. Meteor. Climatol.*, **47**, 1940–1961.
- Kumjian, M. R. and A. V. Ryzhkov, 2009: Storm-relative helicity revealed from polarimetric radar measurements. *J. Atmos. Sci.*, **66**, 667–685.
- Kumjian, M. R. and A. V. Ryzhkov, 2012: The impact of size sorting on the polarimetric radar variables. *J. Atmos. Sci.*, **69**, 2042–2060.
- Lim, K.-S. S. and S.-Y. Hong, 2010: Development of an Effective Double-Moment Cloud Microphysics Scheme with Prognostic Cloud Condensation Nuclei (CCN) for Weather and Climate Models. *Mon. Wea. Rev.*, **138**, 1587–1612.
- Lin, Y.-L., R. D. Farley, and H. D. Orville, 1983: Bulk parameterization of the snow field in a cloud model. *J. Climat. Appl. Meteor.*, **22**, 1065–1092.
- Loney, M. L., D. S. Zrnić, J. M. Straka, and A. V. Ryzhkov, 2002: Enhanced Polarimetric Radar Signatures above the Melting Level in a Supercell Storm. *J. Appl. Meteor.*, **41**, 1179–1194.
- Mansell, E. R., 2010: On sedimentation and advection in multimoment bulk microphysics. *J. Atmos. Sci.*, **67**, 3084–3094.
- Mansell, E. R. and C. L. Ziegler, 2013: Aerosol effects on simulated storm electrification and precipitation in a two-moment bulk microphysics model. *J. Atmos. Sci.*, **70**, 2032–2050.
- Mansell, E. R., C. L. Ziegler, and E. C. Bruning, 2010: Simulated electrification of a small thunderstorm with two-moment bulk microphysics. *J. Atmos. Sci.*, **67**, 171–194.
- Meyers, M. P., R. L. Walko, J. R. Harrington, and W. R. Cotton, 1997: New RAMS cloud microphysics parameterization. Part II: The two-moment scheme. *Atmos. Res.*, **45**, 3–39.
- Milbrandt, J. A. and M. K. Yau, 2005a: A multi-moment bulk microphysics parameterization. Part II: A proposed three-moment closure and scheme description. *J. Atmos. Sci.*, **62**, 3065–3081.
- Milbrandt, J. A. and M. K. Yau, 2005b: A multi-moment bulk microphysics parameterization. Part I: Analysis of the role of the spectral shape parameter. *J. Atmos. Sci.*, **62**, 3051–3064.
- Milbrandt, J. A. and M. K. Yau, 2006: A multimoment bulk microphysics parameterization. Part IV: Sensitivity experiments. *J. Atmos. Sci.*, **63**, 3137–3159.
- Milbrandt, J. A. and R. McTaggart-Cowan, 2010: Sedimentation-induced errors in bulk microphysics schemes. *J. Atmos. Sci.*, **67**, 3931–3948.
- Molthan, A. L. and B. A. Colle, 2012: Comparisons of single- and double-moment microphysics schemes in the simulation of a synoptic-scale snowfall event. *Mon. Wea. Rev.*, **140**, 2982–3002.
- Morrison, H. and J. Milbrandt, 2011: Comparison of two-moment bulk microphysics schemes in idealized supercell thunderstorm simulations. *Mon. Wea. Rev.*, **139**, 1103–1130.
- Morrison, H., G. Thompson, and V. Tatarskii, 2009: Impact of cloud microphysics on the development of trailing stratiform precipitation in a simulated squall line: Comparison of one- and two-moment schemes. *Mon. Wea. Rev.*, **137**, 991–1007.
- Morrison, H., J. A. Milbrandt, G. H. Bryan, K. Ikeda, S. A. Tessendorf, and G. Thompson, 2015: Parameterization of cloud microphysics based on the prediction of bulk ice particle properties. Part II: Case study comparisons with observations and other schemes. *J. Atmos. Sci.*, **72**, 312–339.
- Potvin, C. K., L. J. Wicker, M. I. Biggerstaff, D. Betten, and A. Shapiro, 2013: Comparison between dual-Doppler and EnKF storm-scale wind analyses: The 29–30 May 2004 Geary, Oklahoma, supercell thunderstorm. *Mon. Wea. Rev.*, **141**, 1612–1628.

- Putnam, B. J., M. Xue, Y. Jung, N. A. Snook, and G. Zhang, 2014: The analysis and prediction of microphysical states and polarimetric radar variables in a mesoscale convective system using double-moment microphysics, multinet radar data, and the ensemble Kalman filter. *Mon. Wea. Rev.*, **142**, 141–162.
- Rasmussen, R. M. and and, 1987: Melting and shedding of graupel and hail. Part I: Model physics. *J. Atmos. Sci.*, **44**, 2754–2763.
- Rasmussen, R. M., V. Levizzani, and H. R. Pruppacher, 1984: A wind tunnel and theoretical study on the melting behavior of atmospheric ice particles: III. Experiment and theory for spherical ice particles of radius $> 500 \mu\text{m}$. *J. Atmos. Sci.*, **41**, 381–388.
- Romine, G. S., D. W. Burgess, and R. B. Wilhelmson, 2008: A dual-polarization-radar-based assessment of the 8 May 2003 Oklahoma City area tornadic supercell. *Mon. Wea. Rev.*, **136**, 2849–2870.
- Rotunno, R. and J. B. Klemp, 1982: The influence of the shear-induced pressure gradient on thunderstorm motion. *Mon. Wea. Rev.*, **110**, 136–151.
- Rutledge, S. A. and P. V. Hobbs, 1983: The mesoscale and microscale structure and organization of clouds and precipitation in midlatitude cyclones. VIII: A model for the “seeder-feeder” process in warm-frontal rainbands. *J. Atmos. Sci.*, **40**, 1185–1206.
- Rutledge, S. A. and P. V. Hobbs, 1984: The mesoscale and microscale structure and organization of clouds and precipitation in midlatitude cyclones. XII: A diagnostic modeling study of precipitation development in narrow cold-frontal rainbands. *J. Atmos. Sci.*, **41**, 2949–2972.
- Ryzhkov, A. V., T. J. Schuur, D. W. Burgess, and D. S. Zrníc, 2005: Polarimetric tornado detection. *Journal of Applied Meteorology*, **44**, 557–570.
- Schuur, T. J., A. V. Ryzhkov, P. L. Heinselman, D. S. Zrníc, D. W. Burgess, and K. A. Scharfenberg, 2003: Observations and classifications of echoes with the polarimetric WSR-88D radar., 46 pp.
- Skamarock, W. C., J. B. Klemp, J. Dudhia, D. O. Gill, D. M. Barker, M. G. Duda, X.-Y. Huang, W. Wang, and J. G. Powers, 2008: A description of the Advanced Research WRF version 3. NCAR Tech. Note NCAR/TN-475+STR, 125 pp.
- Straka, J. M. and E. R. Mansell, 2005: A bulk microphysics parameterization with multiple ice precipitation categories. *J. Appl. Meteor.*, **44**, 445–466.
- Straka, J. M., D. S. Zrníc, and A. V. Ryzhkov, 2000: Bulk hydrometeor classification and quantification using polarimetric radar data: Synthesis of relations. *Journal of Applied Meteorology*, **39**, 1341–1372.
- Tao, W.-K. and J. Simpson, 1993: Goddard cumulus ensemble model. Part I: Model description. *Terres. Atmos. Ocean Sci.*, **4**, 35–72.
- Thompson, G., P. R. Field, R. M. Rasmussen, and W. D. Hall, 2008: Explicit forecasts of winter precipitation using an improved bulk microphysics scheme. Part II: Implementation of a new snow parameterization. *Mon. Wea. Rev.*, **136**, 5095–5115.
- Thwaites, S., J. N. Carras, and W. C. Macklin, 1977: The aerodynamics of oblate hailstones. *Quart. J. Roy. Meteor. Soc.*, **103**, 803–808.
- Van Weverberg, K., A. M. Vogelmann, H. Morrison, and J. A. Milbrandt, 2012: Sensitivity of idealized squall-line simulations to the level of complexity used in two-moment bulk microphysics schemes. *Mon. Wea. Rev.*, **140**, 1883–1907.
- Van Weverberg, K., A. M. Vogelmann, W. Lin, E. P. Luke, A. Cialella, P. Minnis, M. Khaiyer, E. R. Boer, and M. P. Jensen, 2013: The role of cloud microphysics parameterization in the simulation of mesoscale convective system clouds and precipitation in the tropical western

- Pacific. *J. Atmos. Sci.*, **70**, 1104–1128.
- Vivekanandan, J., W. M. Adams, and V. N. Bringi, 1991: Rigorous approach to polarimetric radar modeling of hydrometeor orientation distributions. *Journal of Applied Meteorology*, **30**, 1053–1063.
- Wacker, U. and A. Seifert, 2001: Evolution of rain water profiles resulting from pure sedimentation: Spectral vs. parameterized description. *Atmos. Res.*, **58**, 19–39.
- Waterman, P. C., 1969: Scattering by dielectric obstacles. *Alta Freq.*, **38**, 348–352.
- Weisman, M. L. and J. B. Klemp, 1982: The dependence of numerically simulated convective storms on vertical wind shear and buoyancy. *Mon. Wea. Rev.*, **110**, 504–520.
- Weisman, M. L., W. C. Skamarock, and J. B. Klemp, 1997: The resolution dependence of explicitly modeled convective systems. *Mon. Wea. Rev.*, **125**, 527–548.
- Xue, M., Y. Jung, and G. Zhang, 2010a: State estimation of convective storms with a two-moment microphysics scheme and an ensemble Kalman filter: Experiments with simulated radar data *Quart. J. Roy. Meteor. Soc.*, **136**, 685–700.
- Xue, M., F. Kong, K. W. Thomas, J. Gao, Y. Wang, K. Brewster, K. K. Droegemeier, J. Kain, S. Weiss, D. Bright, M. Coniglio, and J. Du, 2008: CAPS realtime storm-scale ensemble and high-resolution forecasts as part of the NOAA Hazardous Weather Testbed 2008 Spring Experiment. *24th Conf. on Several Local Storms*, Savannah, GA, Amer. Meteor. Soc., 12.2.
- Xue, M., F. Kong, D. Weber, K. W. Thomas, Y. Wang, K. Brewster, K. K. Droegemeier, J. S. Kain, S. J. Weiss, D. R. Bright, M. S. Wandishin, M. C. Coniglio, and J. Du, 2007: CAPS realtime storm-scale ensemble and high-resolution forecasts as part of the NOAA Hazardous Weather Testbed 2007 spring experiment. *22nd Conf. on Weather Analysis and Forecasting/18th Conf. on Numerical Weather Prediction*, Park City, Utah, Amer. Meteor. Soc., 3B.1.
- Xue, M., F. Kong, K. W. Thomas, Y. Wang, K. Brewster, J. Gao, X. Wang, S. J. Weiss, A. J. Clark, J. S. Kain, M. C. Coniglio, J. Du, T. L. Jensen, and Y. H. Kuo, 2010b: CAPS realtime storm-scale ensemble and convection-resolving high-resolution forecasts for the NOAA Hazardous Weather Testbed 2010 spring experiment. *25th Conf. on Severe Local Storms*, Denver, CO, Amer. Meteor. Soc., 7B.3.
- Yuter, S. A. and R. A. Houze, Jr., 1995: Three-dimensional kinematic and microphysical evolution of Florida cumulonimbus. Part II: Frequency distributions of vertical velocity, reflectivity, and differential reflectivity. *Mon. Wea. Rev.*, **123**, 1941–1963.
- Zhang, G., J. Vivekanandan, and E. Brandes, 2001: A method for estimating rain rate and drop size distribution from polarimetric radar measurements. *IEEE Trans. Geosci. Remote Sens.*, **39**, 830–841.
- Ziegler, C. L., 1985: Retrieval of thermal and microphysical variables in observed convective storms. Part I: Model development and preliminary testing. *J. Atmos. Sci.*, **42**, 1487–1509.

Table 1. Example references of observed polarimetric signatures examined in this paper.

Observed polarimetric signatures	References
Z_{DR} column	Illingworth et al. (1987); Conway and Zrnic (1993); Brandes et al. (1995); Loney et al. (2002)
K_{DP} column	Hubbert et al. (1998); Loney et al. (2002)
Z_{DR} arc	Ryzhkov et al. (2005); KR08; KR09
Midlevel Z_{DR}/ρ_{HV} rings	KR08
Hail signature in forward flank downdraft	KR08
K_{DP} foot	Romine et al. (2008)

Table 2. WRF model input.

WRF Model Configuration	
Run time	180 min.
Δt	6 s
Sound wave Δt	1 s
Model output interval	10 min.
Horizontal domain	199 km x 199 km
Model lid	20 km
Δx	1 km
Δy	1 km
Δz	~500 m
Time integration scheme	3 rd order Runge-Kutta
Horizontal momentum advection	5 th order
Vertical momentum advection	3 rd order
Horizontal scalar advection	5 th order
Vertical scalar advection	3 rd order
Upper level damping	5000 m below model top
Rayleigh damping coefficient	0.003
Horizontal boundary conditions	Open

Table 3. Predicted moments in the microphysics schemes evaluated in this study. q denotes mass mixing ratio, while N_t denotes total number concentration. A hydrometeor category that is not included in a microphysics scheme is listed as not applicable (NA).

	Morrison	MY2	NSSL	Thompson	WDM6
Cloud Droplets	q	q, N_t	q, N_t	q	q, N_t
Rain	q, N_t				
Cloud Ice	q, N_t	q, N_t	q, N_t	q, N_t	q
Snow	q, N_t	q, N_t	q, N_t	q	q
Graupel	q, N_t	q, N_t	q, N_t	q	q
Hail	NA	q, N_t	q, N_t	NA	NA

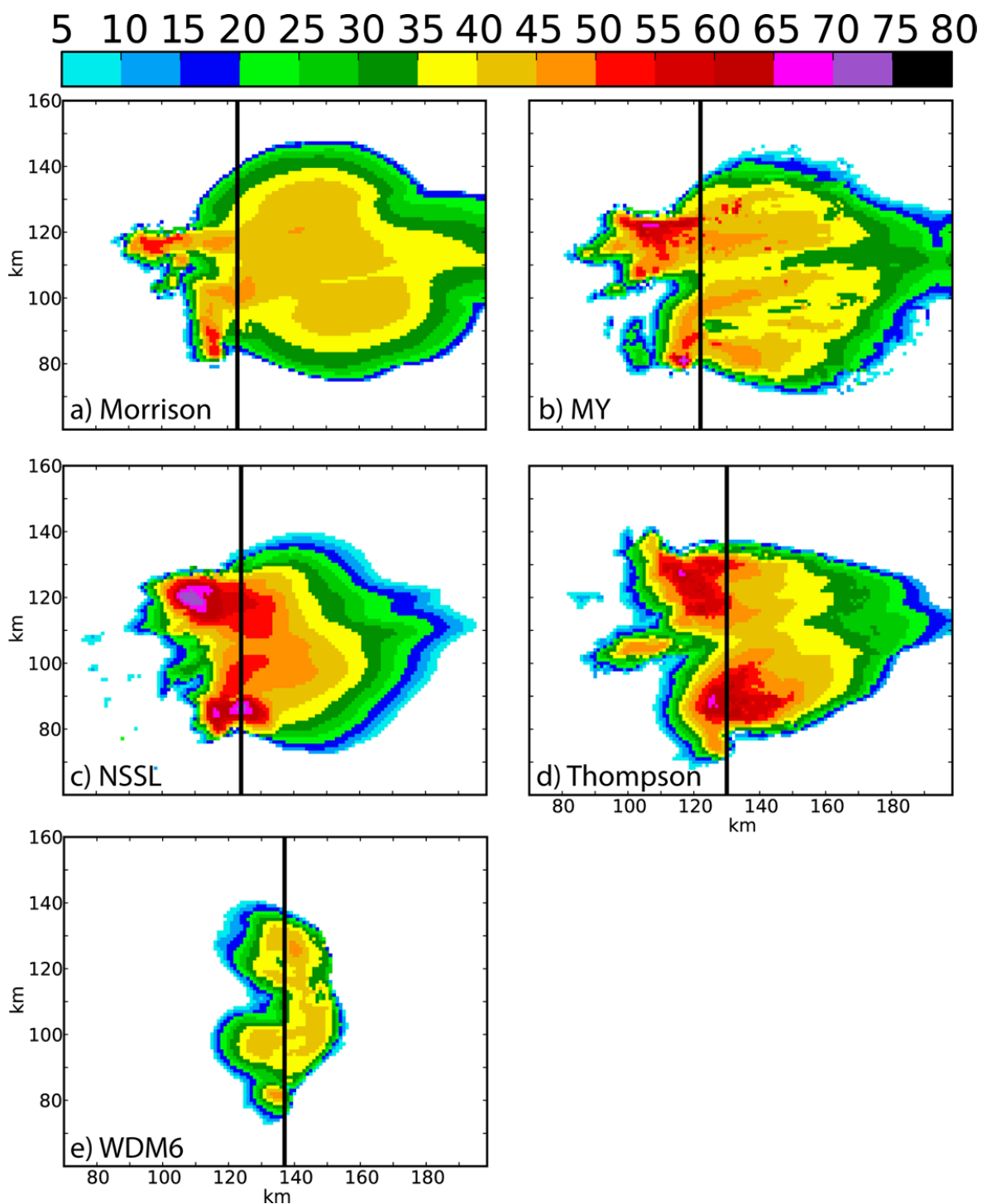


Fig. 1. Z_H (dBZ) at $z \approx 250$ m for the (a) Morrison, (b) MY2, (c) NSSL, and (d) Thompson schemes at $t = 100$ min., and the (e) WDM6 scheme at $t = 120$ min. Black lines show where vertical cross sections for each microphysics scheme are taken.

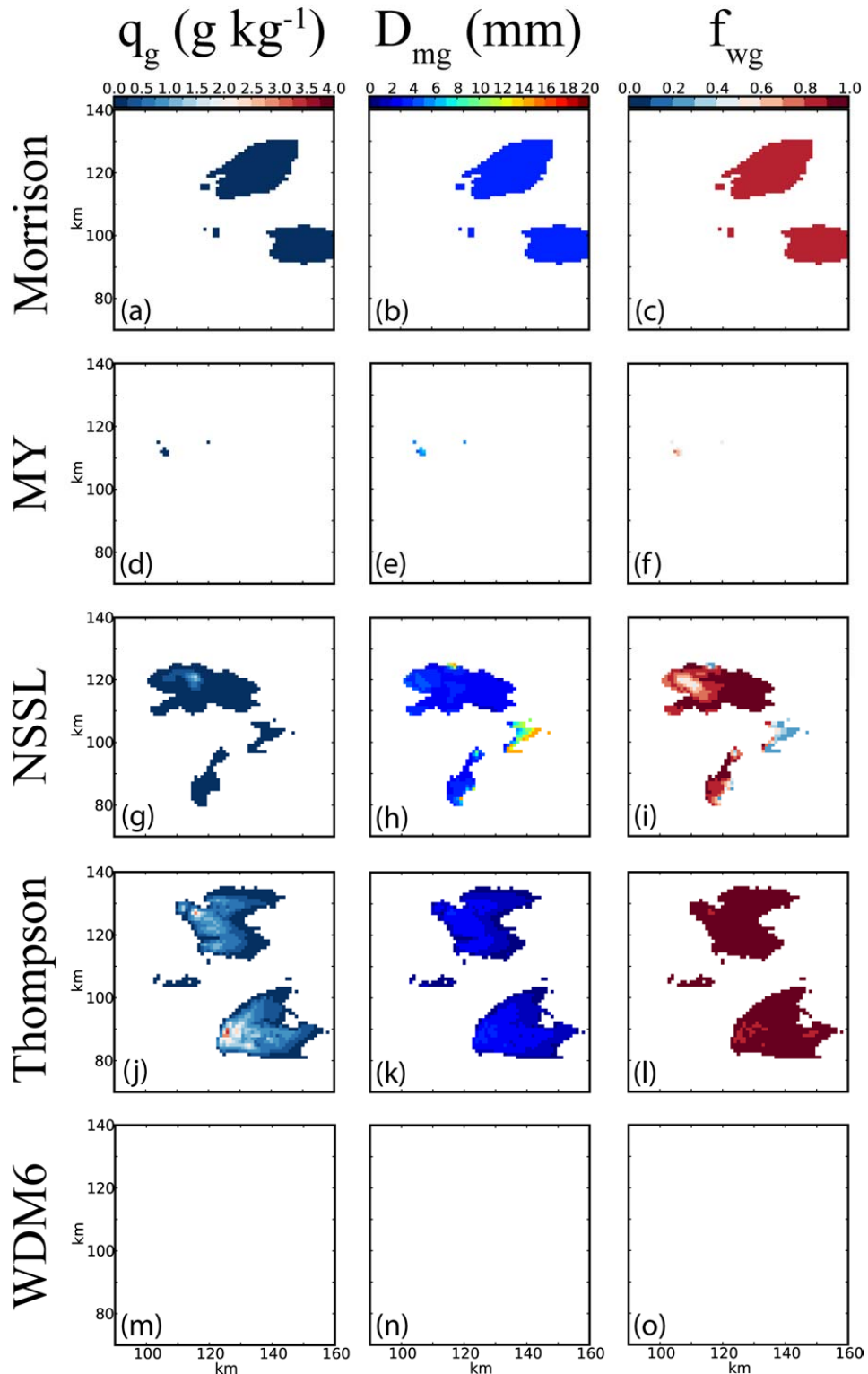


Fig. 2. q_g (g kg^{-1}), D_{mg} (mm), and f_{wg} at $z \sim 250$ m for the (a)-(c) Morrison, (d)-(f) MY2, (g)-(i) NSSL, and (j)-(l) Thompson schemes at $t = 100$ min., and the (m)-(o) WDM6 scheme at $t = 120$ min.

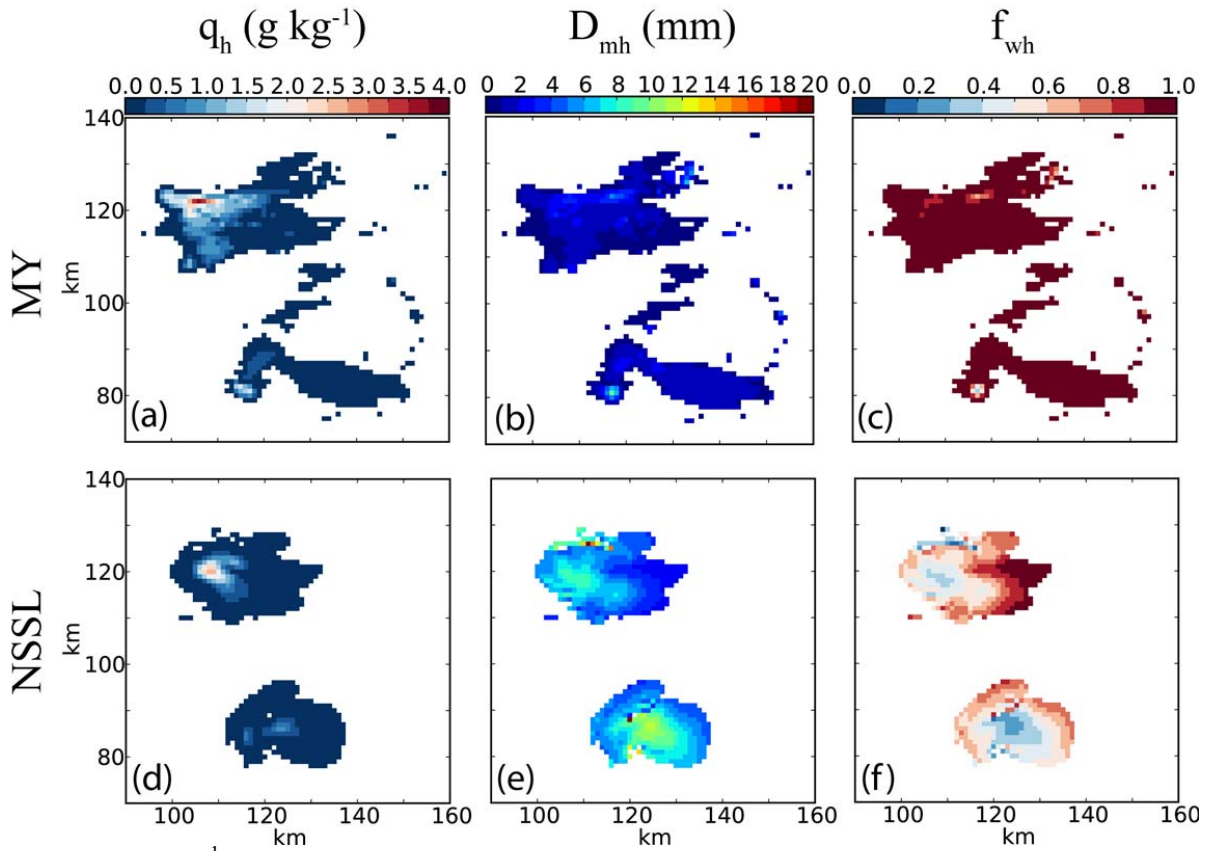


Fig. 3. q_h (g kg^{-1}), D_{mh} (mm), and f_{wh} at $z \approx 250$ m for the (a)-(c) MY2 and (d)-(f) NSSL schemes at $t = 100$ min.

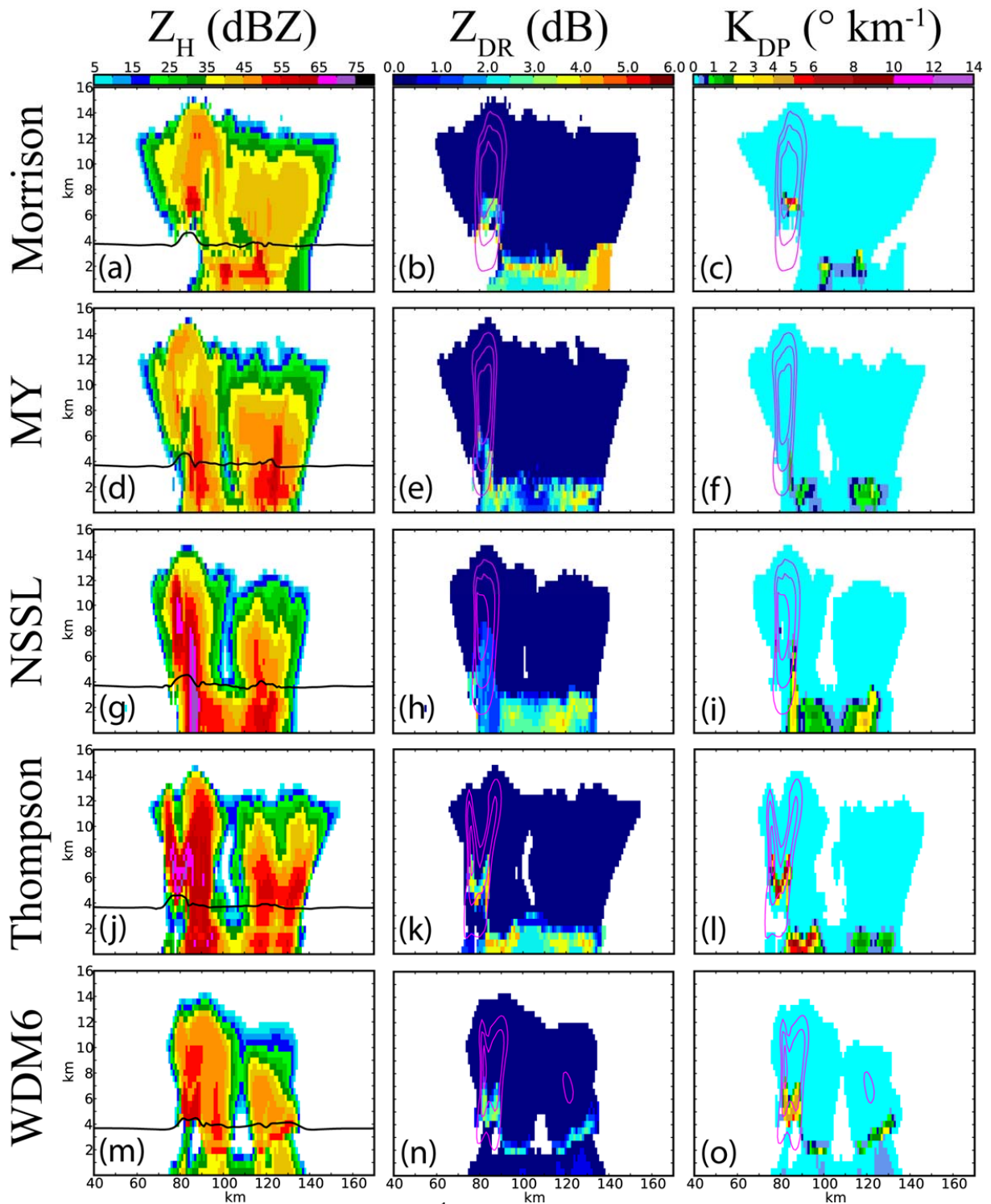


Fig. 4. Z_H (dBZ), Z_{DR} (dB), and K_{DP} ($^{\circ} \text{ km}^{-1}$) columns for the (a)-(c) Morrison, (d)-(f) MY2, (g)-(i) NSSL, and (j)-(l) Thompson schemes at $t = 100$ min., and the (m)-(o) WDM6 scheme at $t = 120$ min. Vertical velocity contours are shown in Z_{DR} and K_{DP} plots with contours of 15 m s^{-1} starting from 10 m s^{-1} . The 0°C isotherm is shown in Z_H plots.

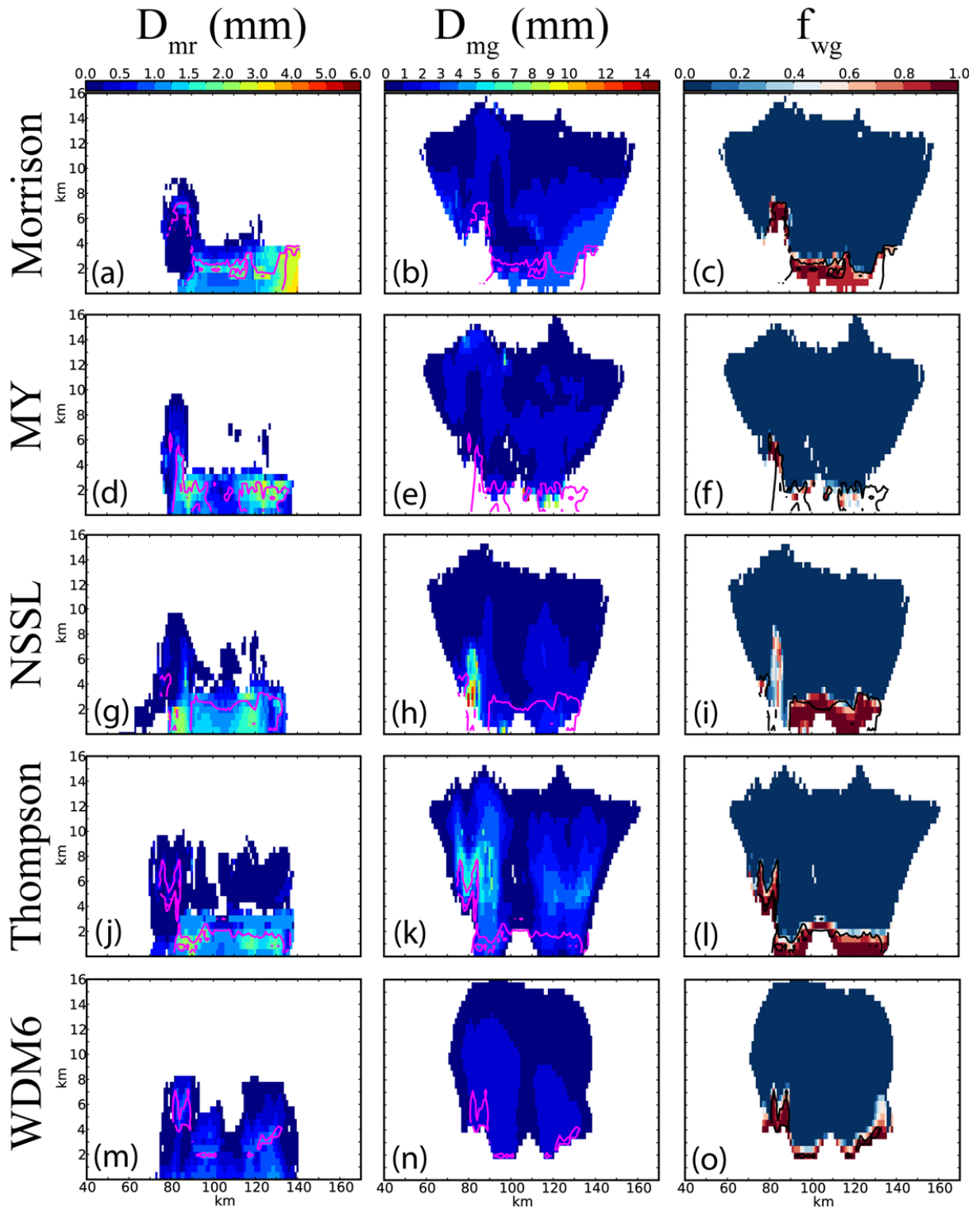


Fig. 5. D_{mr} (mm), D_{mg} (mm), and f_{wg} as in Fig. 4. Z_{DR} (dB; magenta in D_m plots, black in f_{wg} plots) contours are shown for the 2 and 4 dB levels.

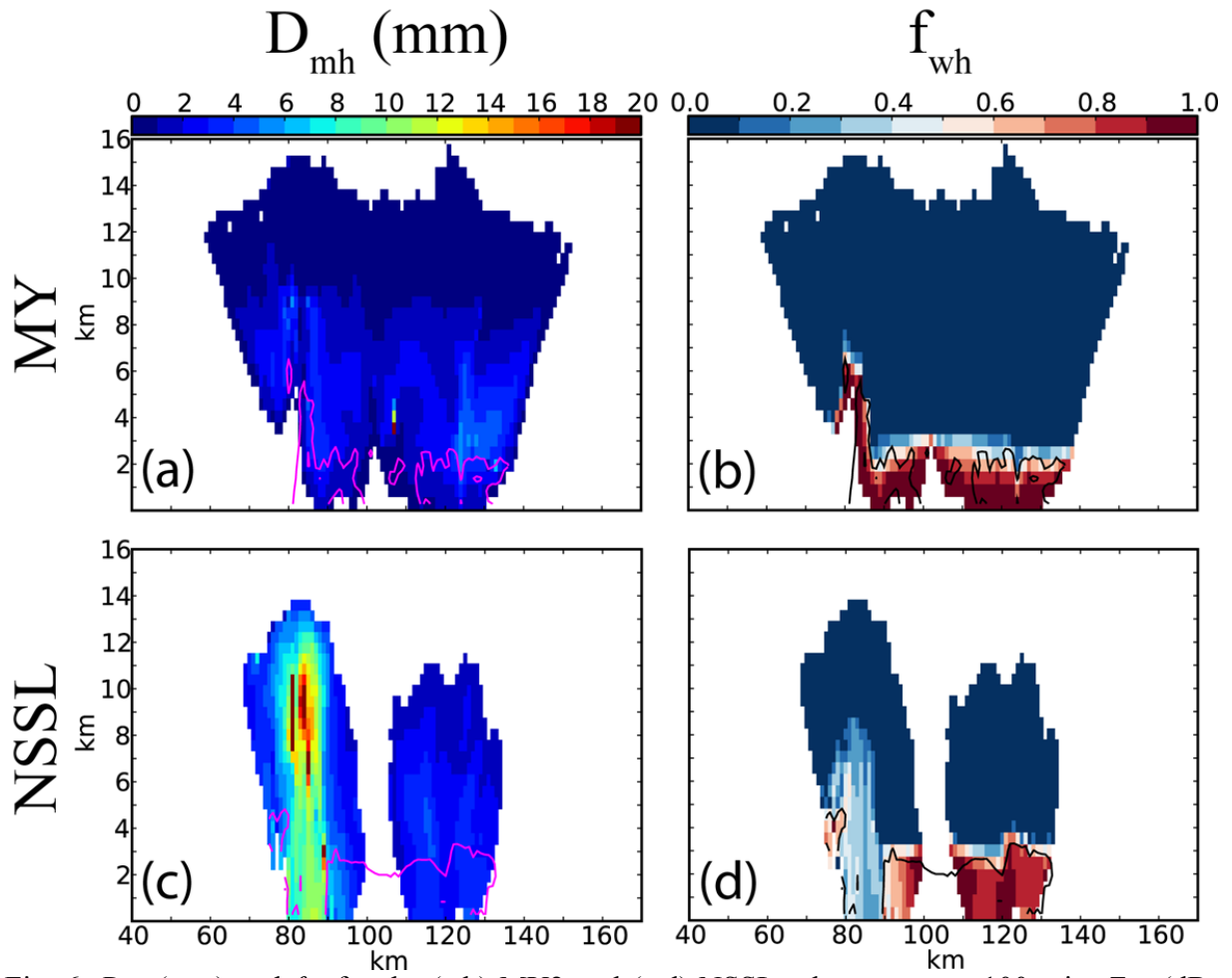


Fig. 6. D_{mh} (mm) and f_{wh} for the (a,b) MY2 and (c,d) NSSL schemes at $t = 100$ min. Z_{DR} (dB; magenta in D_{mh} plots, black in f_{wh} plots) contours are shown for the 2 and 4 dB levels.

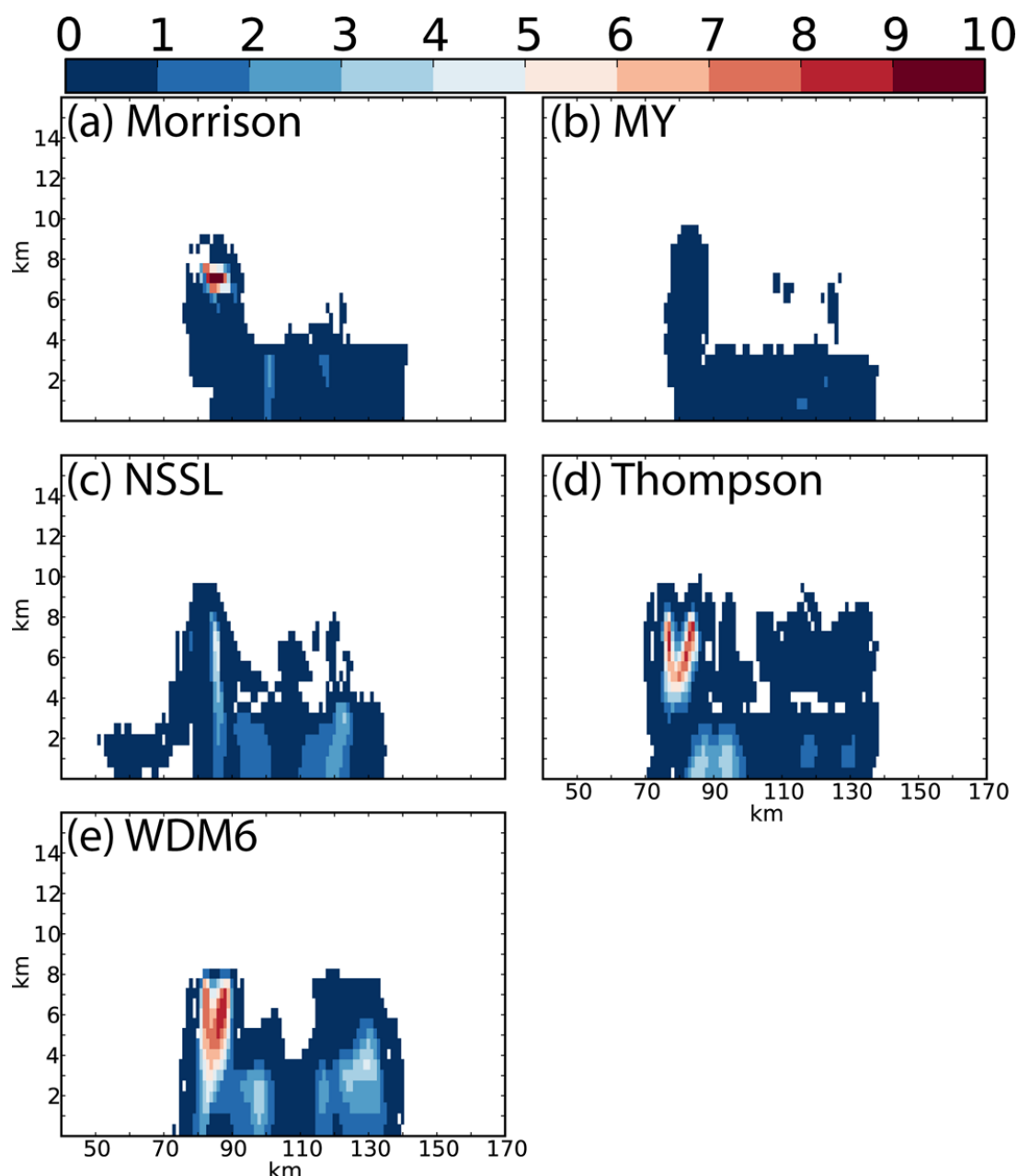


Fig. 7. q_r (g kg^{-1}) for the (a) Morrison, (b) MY2, (c) NSSL, and (d) Thompson schemes at $t = 100$ min., and for the (e) WDM6 scheme at $t = 120$ min.

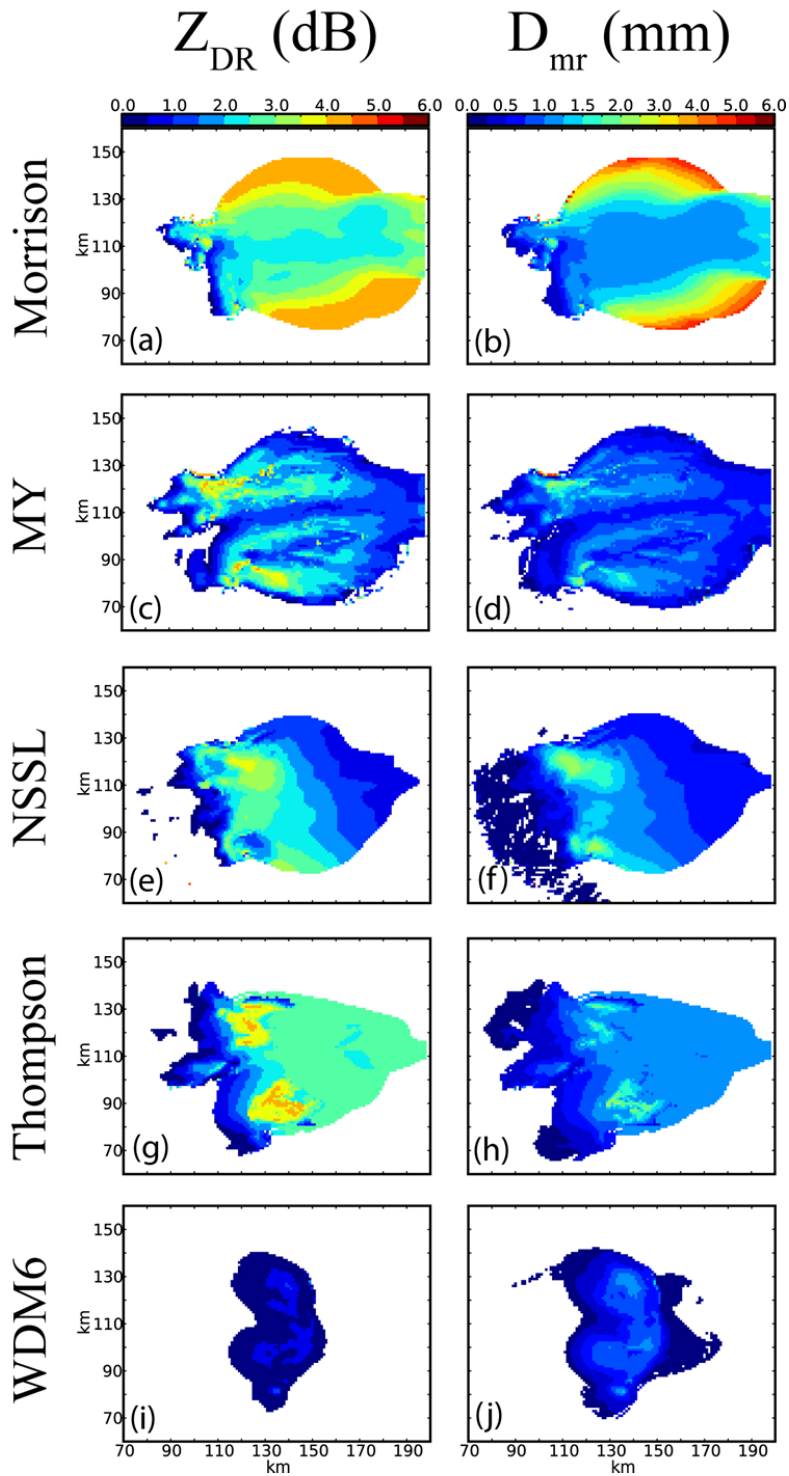


Fig. 8. Z_{DR} (dB) and D_{mr} (mm) at $z \approx 250$ m showing Z_{DR} arcs for the (a,b) Morrison, (c,d) MY2, (e,f) NSSL, and (g,h) Thompson schemes at $t = 100$ min., and the (i,j) WDM6 scheme at $t = 120$ min.

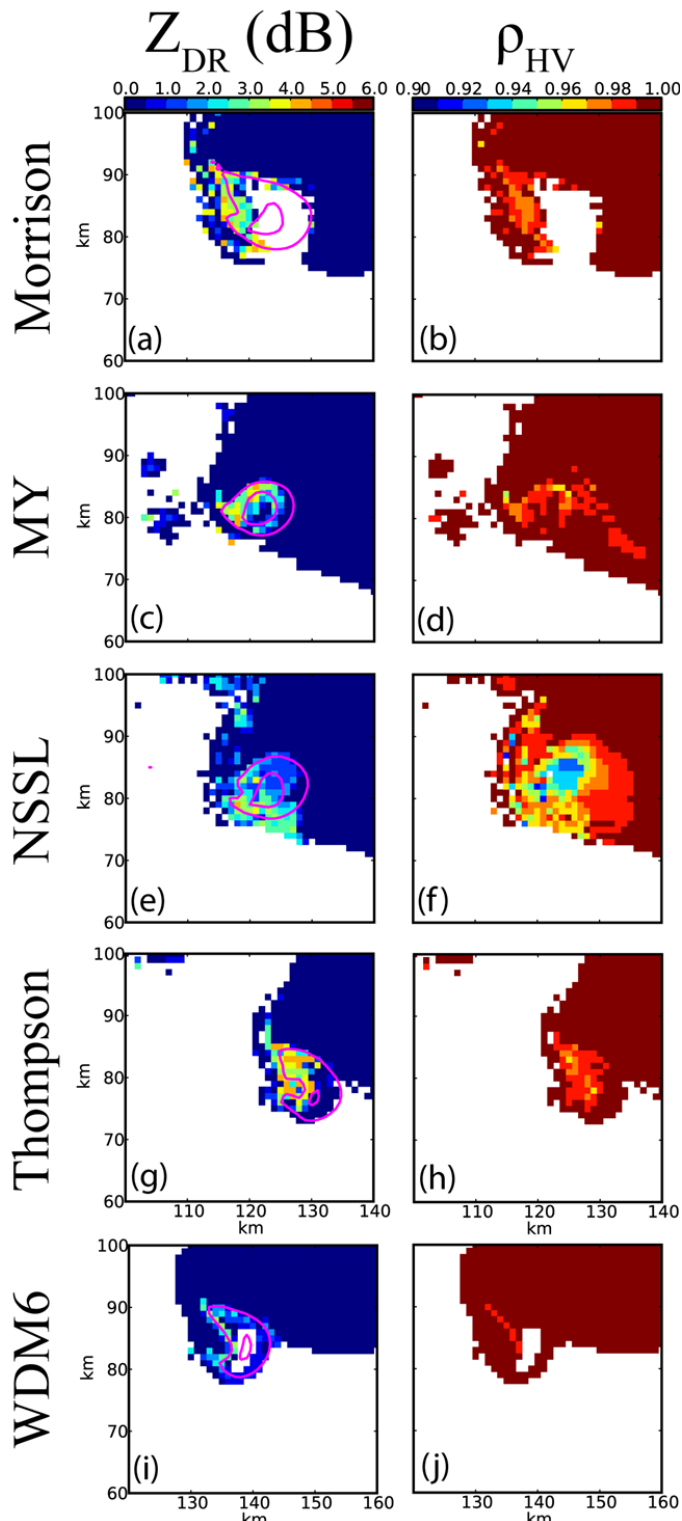


Fig. 9. Midlevel Z_{DR} (dB) and ρ_{hv} at $z \approx 4$ km for the (a,b) Morrison, (c,d) MY2, (e,f) NSSL, and (g,h) Thompson schemes at $t = 100$ min., and the (i,j) WDM6 scheme at $t = 120$ min. Vertical velocity contours are shown in Z_{DR} plots with contours of 15 m s^{-1} starting from 10 m s^{-1} .

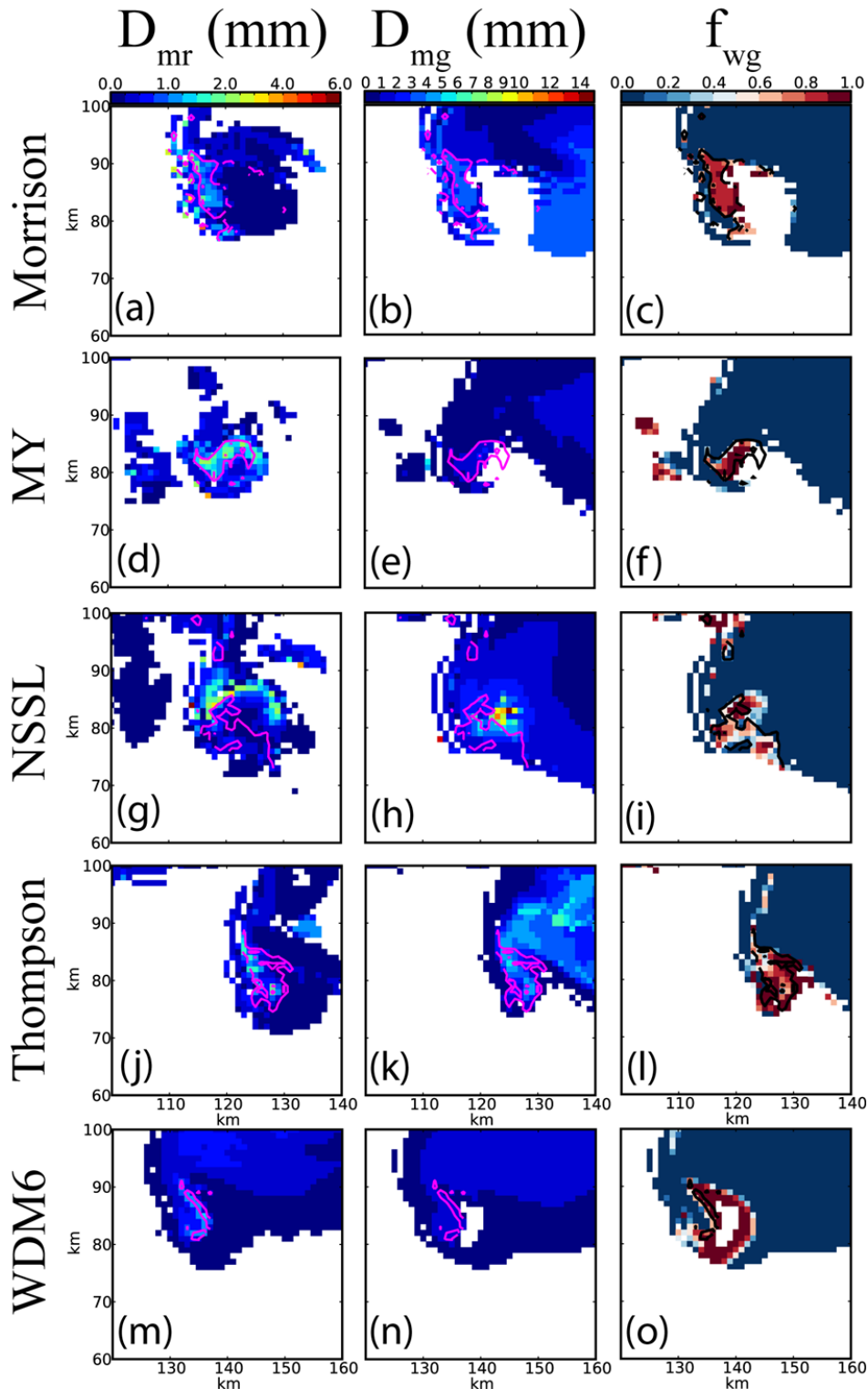


Fig. 10. Midlevel D_{mr} (mm), D_{mg} (mm), and f_{wg} at $z = \sim 4$ km for the (a)-(c) Morrison, (d)-(f) MY2, (g)-(i) NSSL, and (j)-(l) Thompson schemes at $t = 100$ min., and the (m)-(o) WDM6 scheme at $t = 120$ min. Z_{DR} (dB; magenta in D_m plots, black in f_{wg} plots) contours are shown for the 2 and 4 dB levels.

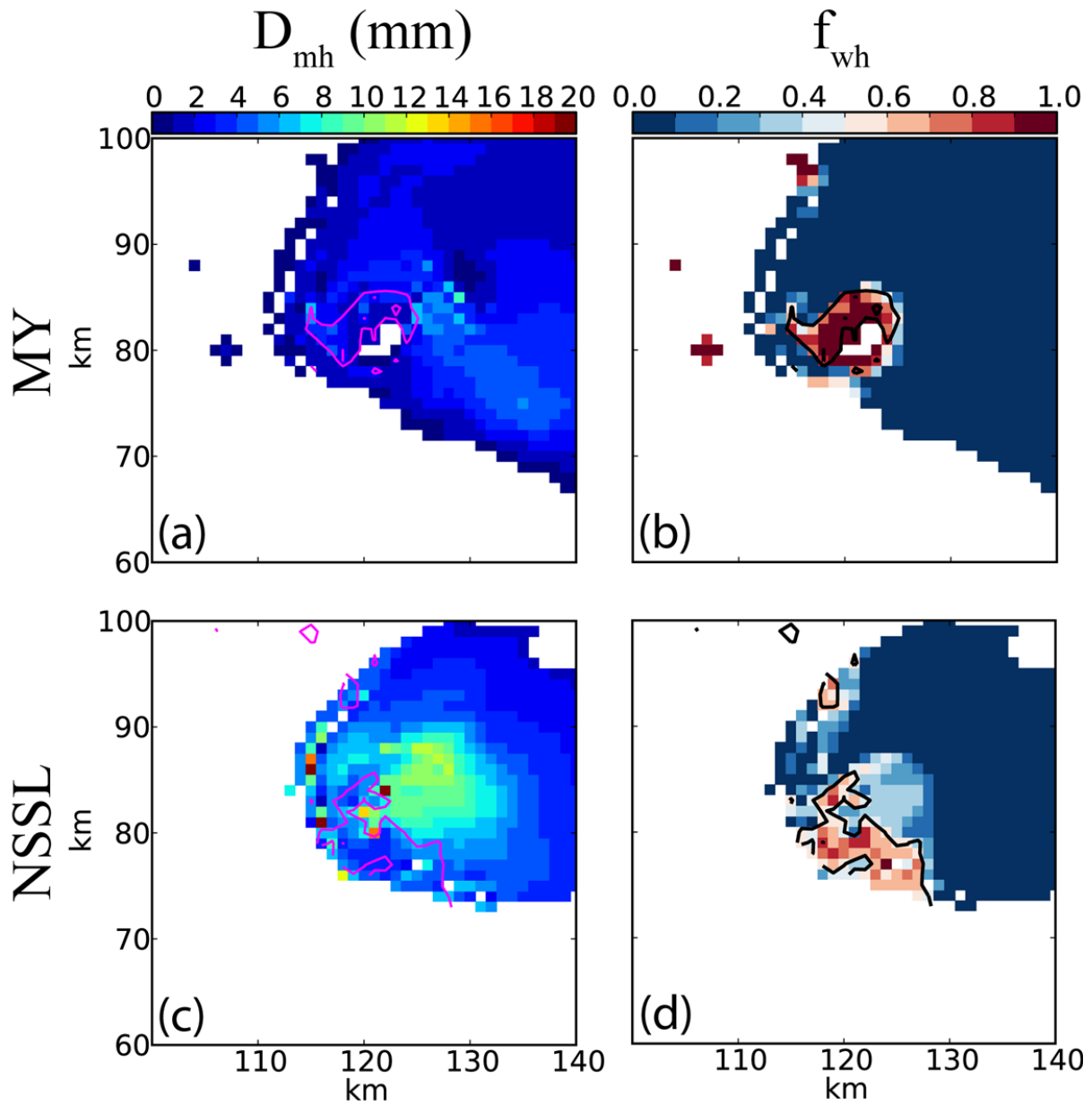


Fig. 11. D_{mh} (mm) and f_{wh} at $z \approx 4$ km for midlevel rings for the (a,b) MY2 and (c,d) NSSL schemes at $t = 100$ min. Z_{DR} (dB; magenta in D_{mh} plots, black in f_{wh} plots) contours are shown for the 2 and 4 dB levels.

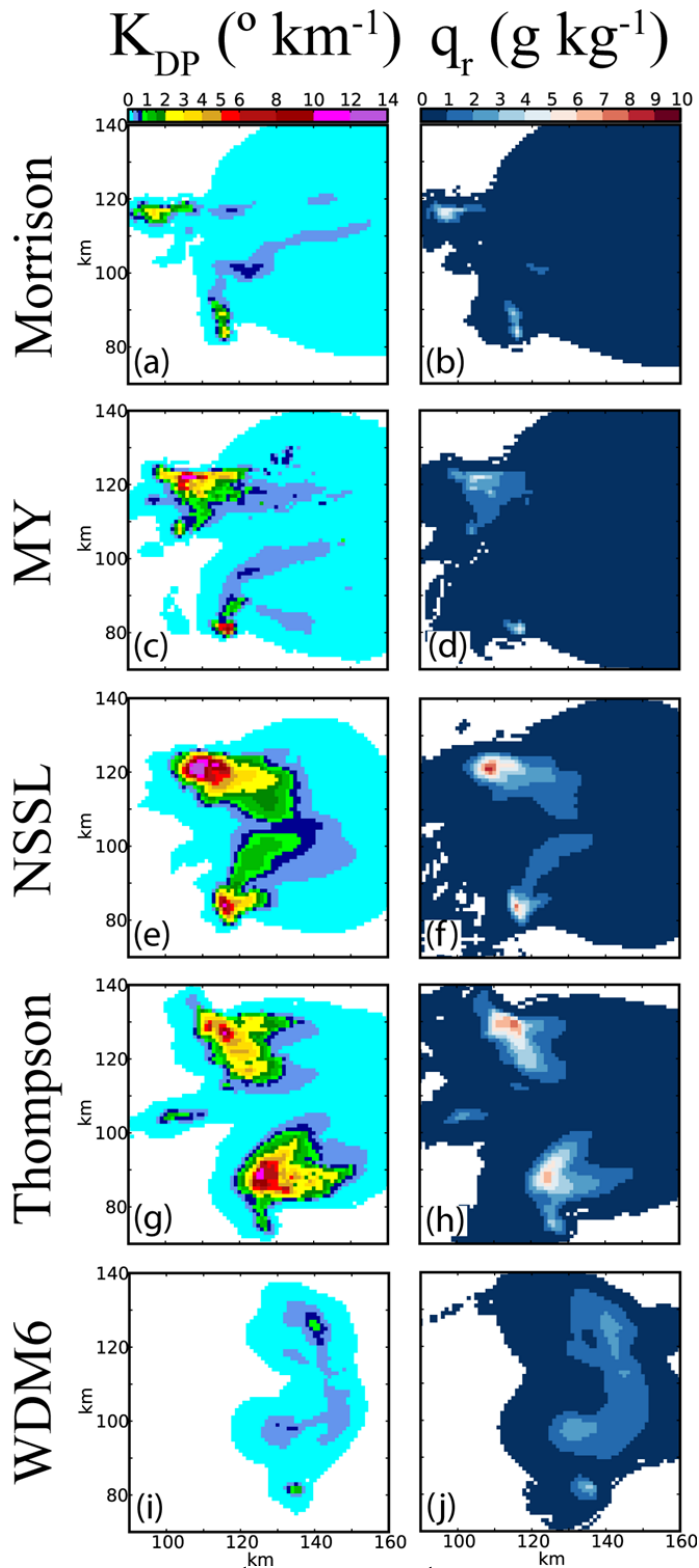


Fig. 12. K_{DP} ($^{\circ} \text{ km}^{-1}$) and q_r (g kg^{-1}) at $z \approx 250$ m for the (a,b) Morrison, (c,d) MY2, (e,f) NSSL, and (g,h) Thompson schemes at $t = 100$ min., and the (i,j) WDM6 scheme at $t = 120$ min.

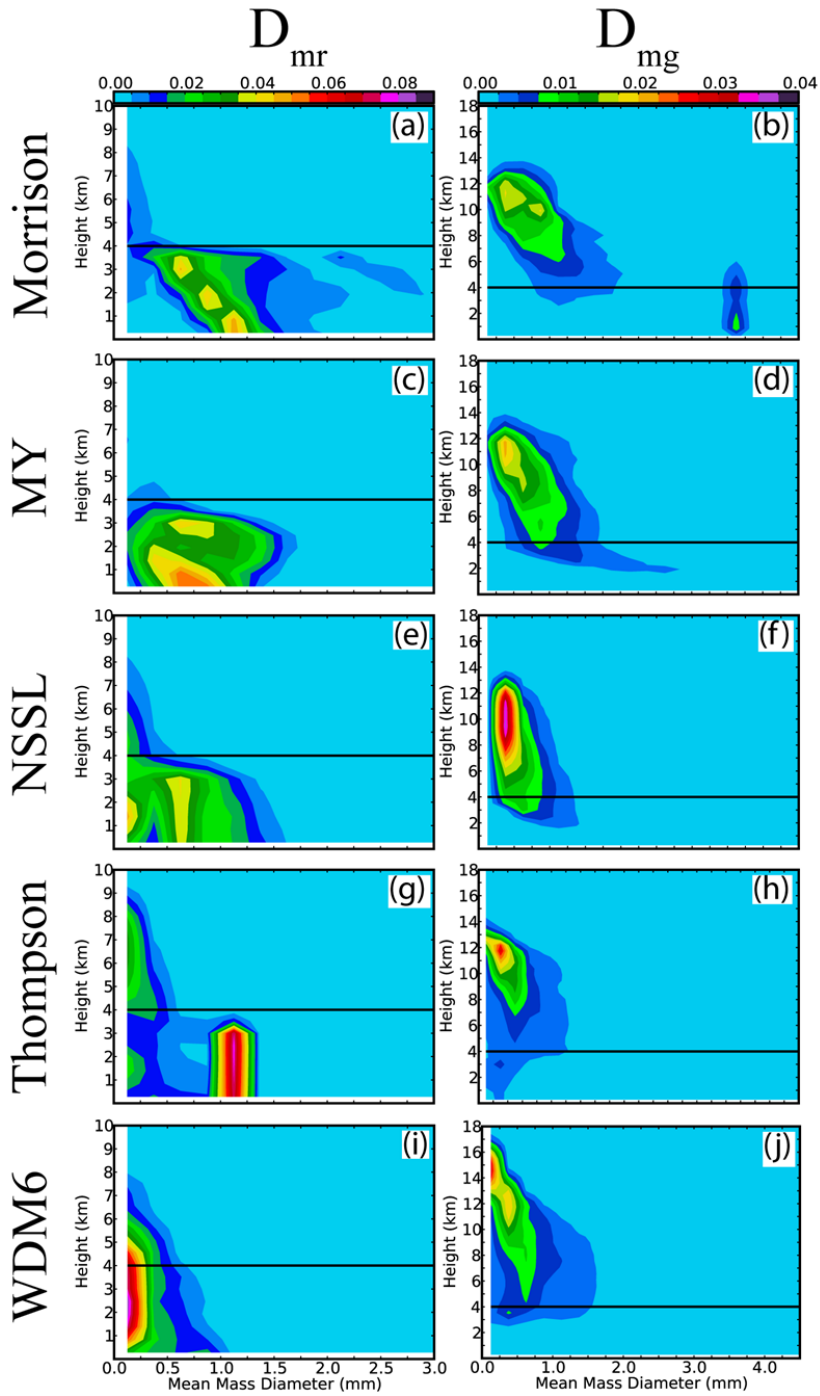


Fig. 13. Rain and graupel CFADs, shown in relation to both D_{mr} and D_{mg} , and height for the (a,b) Morrison, (c,d) MY2, (e,f) NSSL, and (g,h) Thompson schemes at $t = 100$ min., and the (i,j) WDM6 scheme at $t = 120$ min. Approximate melting level is shown at 4 km by horizontal black lines.

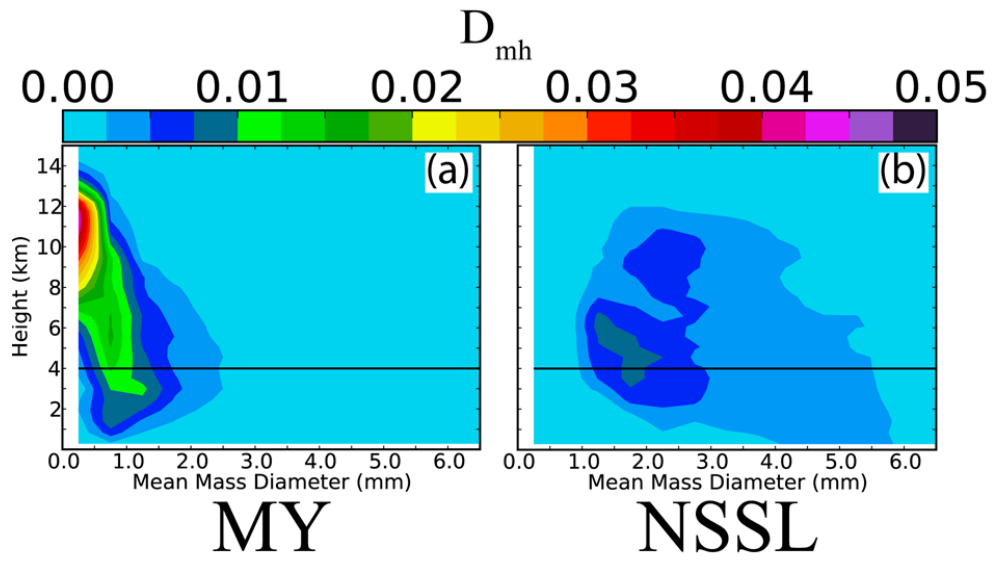


Fig. 14. Hail CFADs, shown in relation to D_{mh} and height for the (a) MY2 and (b) NSSL schemes at $t = 100$ min. Approximate melting level is shown at 4 km by horizontal black lines.